



Supplementary Materials for **Strongly correlated quantum walks with a 12-qubit superconducting processor**

Zhiguang Yan*, Yu-Ran Zhang*, Ming Gong*, Yulin Wu, Yarui Zheng, Shaowei Li, Can Wang, Futian Liang, Jin Lin, Yu Xu, Cheng Guo, Lihua Sun, Cheng-Zhi Peng, Keyu Xia, Hui Deng, Hao Rong, J. Q. You, Franco Nori, Heng Fan†, Xiaobo Zhu†, Jian-Wei Pan

*These authors contributed equally to this work.

†Corresponding author. Email: hfan@iphy.ac.cn (H.F.); xbzhu16@ustc.edu.cn (X.Z.)

Published 2 May 2019 on *Science* First Release
DOI: 10.1126/science.aaw1611

This PDF file includes:

Materials and Methods
Supplementary Text
Figs. S1 to S20
Table S1
Caption for Movie S1
References

Other Supporting Online Material for this manuscript includes the following:
(available at science.sciencemag.org/cgi/content/full/science.aaw1611/DC1)

Movie S1

Contents

I. Experimental device	2
A. Performance	2
B. Fabrication	5
C. Experimental wiring set-up	5
D. Qubit Readout	6
E. Waveform sequences	9
II. Calibration	10
A. Z pulse distortion	10
B. Z pulse crosstalk correction	12
C. Single-qubit rotation gate implementation and optimization	14
III. Adjusting all qubits to the same frequency	14
IV. One-photon quantum walks using eleven superconducting qubits	15
V. The Bose-Hubbard model of the nearest-neighbor coupled transmon qubits	15
A. Derivation of the Bose-Hubbard model	15
B. Fermionization of interacting photons	18
C. The effect of unbalanced qubits' frequencies	18
D. Numerical simulations of continuous-time quantum walks	19
E. The effect of the measurement precision of the nearest-neighbor coupling strength	20
VI. Lieb-Robinson bound	22
VII. Comparison with previous work	22
A. One-photon quantum walks	22
B. Two-photon quantum walks	23
VIII. Extended data	24
References	33

I. EXPERIMENTAL DEVICE

A. Performance

Our experiments are implemented with a superconducting circuit, with twelve cross-shaped transmon qubits of the Xmon variety arranged in a linear array with nearly identical nearest-neighbor couplings via eleven fixed capacitors (Fig. S1), where the quantum coherence of each qubit is improved by a large shunt capacitor [21–23]. As shown in Table S1, $J/2\pi \approx 12.5$ MHz. The readout resonator's frequency $\omega_{\text{read}}/2\pi$ spans from 6.503 to 6.838 GHz, well located within the bandwidth of our Josephson Parametric Amplifier (JPA) [25]. $\omega_{\text{idle}}/2\pi$ is the qubit's idle frequency, adjusted by the Z DC control line. The energy relaxation time T_1 and dephasing time T_2^* of the qubit are measured at the idle point ω_{idle} . The adjacent qubits' sweet point frequencies are designed to have a difference of about 500 MHz. With this frequency difference, we can avoid the XY

Parameters	Q ₁	Q ₂	Q ₃	Q ₄	Q ₅	Q ₆	Q ₇	Q ₈	Q ₉	Q ₁₀	Q ₁₁	Q ₁₂
$\omega_{\text{read}}/2\pi$ (GHz)	6.503	6.538	6.567	6.597	6.640	6.646	6.697	6.730	6.762	6.782	6.812	6.838
$\omega_{\text{max}}/2\pi$ (GHz)	5.436	4.918	5.21	5.026	5.455	4.917	5.514	5.016	5.571	5.018	5.597	5.027
$\omega_{\text{idle}}/2\pi$ (GHz)	5.436	4.760	5.210	4.840	5.300	4.900	5.480	4.940	5.420	4.980	5.520	4.880
T_1 (μs)	12.76	18.2	18.04	14.6	14.34	20.74	17.02	24.62	12.73	10.46	23.19	16.41
T_2^* (μs)	9.3	4.6	20.4	4.3	3.7	14.9	10.8	7.3	3.2	11.5	6.1	4.1
$J/2\pi$ (MHz)		12.1	12.2	12.3	12.4	12.5	12.6	12.6	12.6	12.6	12.5	12.4
$\eta/2\pi$ (MHz)	-246	-204	-246	-200	-248	-196	-248	-196	-246	-214	-244	-200
$\chi_{qr}/2\pi$ (MHz)	0.55	0.17	0.35	0.19	0.39	0.20	0.40	0.22	0.36	0.20	0.36	0.20
f_{00}	0.96	0.95	0.94	0.95	0.95	0.97	0.98	0.97	0.98	0.93	0.97	0.95
f_{11}	0.88	0.86	0.82	0.81	0.84	0.86	0.93	0.88	0.86	0.83	0.83	0.85
Readout visibility	0.84	0.81	0.76	0.76	0.79	0.83	0.91	0.85	0.84	0.76	0.80	0.80
Integration time (ns)	986	1650	1000	1650	936	1500	1250	1750	1500	1750	1750	2000

TABLE S1: Device parameters: $\omega_{\text{read}}/2\pi$ is the frequency of the readout resonator; $\omega_{\text{max}}/2\pi$ is the maximum frequency of the qubit; $\omega_{\text{idle}}/2\pi$ is the qubit's idle frequency; T_1 is the qubit's energy relaxation time; T_2^* is the qubit's dephasing time; J is the nearest-neighbor qubits' coupling strength, of which the values are listed between their neighboring qubits. The on-site nonlinear interaction U equals the qubit's anharmonicity ($\eta \equiv f_{12} - f_{01}$, with f_{12} being the transition frequency between $|1\rangle$ and $|2\rangle$ and f_{01} being the transition frequency between $|0\rangle$ and $|1\rangle$) measured near the idle points, and can be considered a fixed value as it is almost constant with the qubit frequency; χ_{qr} is the dispersive shift; f_{00} (f_{11}) is the probability of correctly identifying the qubit state when it is prepared in $|0\rangle$ ($|1\rangle$). The integration time for the measurements of each qubit ranges from 986 ns to 2000 ns, which results from the optimization of the readout visibility.

crosstalk-induced unwanted excitation, when adjacent qubits are near their sweet points. This also helps to avoid the direct coupling between adjacent qubits, when they are both idled around their sweet points. For our qubit, the m -th eigenenergy is approximately given by

$$E_m \simeq -E^J + \sqrt{8E^C E^J}(m + 1/2) - E^C(m^2 + m + 1/2)/2. \quad (\text{S1})$$

The Josephson energies E^J can be controlled by changing the area of the Josephson junctions. Controlling the capacitors shunted to the Josephson junctions is much easier during fabrication. Therefore, we choose to keep the area of the Josephson junctions to be the smallest and the same for all qubits to reduce the density of two-level systems coupled to the qubits, i.e. the E^J for different qubits are the same. The charging energy E^C , controlled by the capacitors shunted to the Josephson junctions, are designed to be in two groups. For odd and even qubits, E^C are designed to be around 250 MHz and 200 MHz, respectively; and the sweet point frequencies are designed to be around 5.5 GHz and 5.0 GHz, respectively. A micrograph and simplified schematic circuit of the device are shown in Fig. S1.

To obtain the coupling strength between the neighboring qubits, we measure the vacuum Rabi oscillations between these neighboring qubits when they are biased to the working point. The

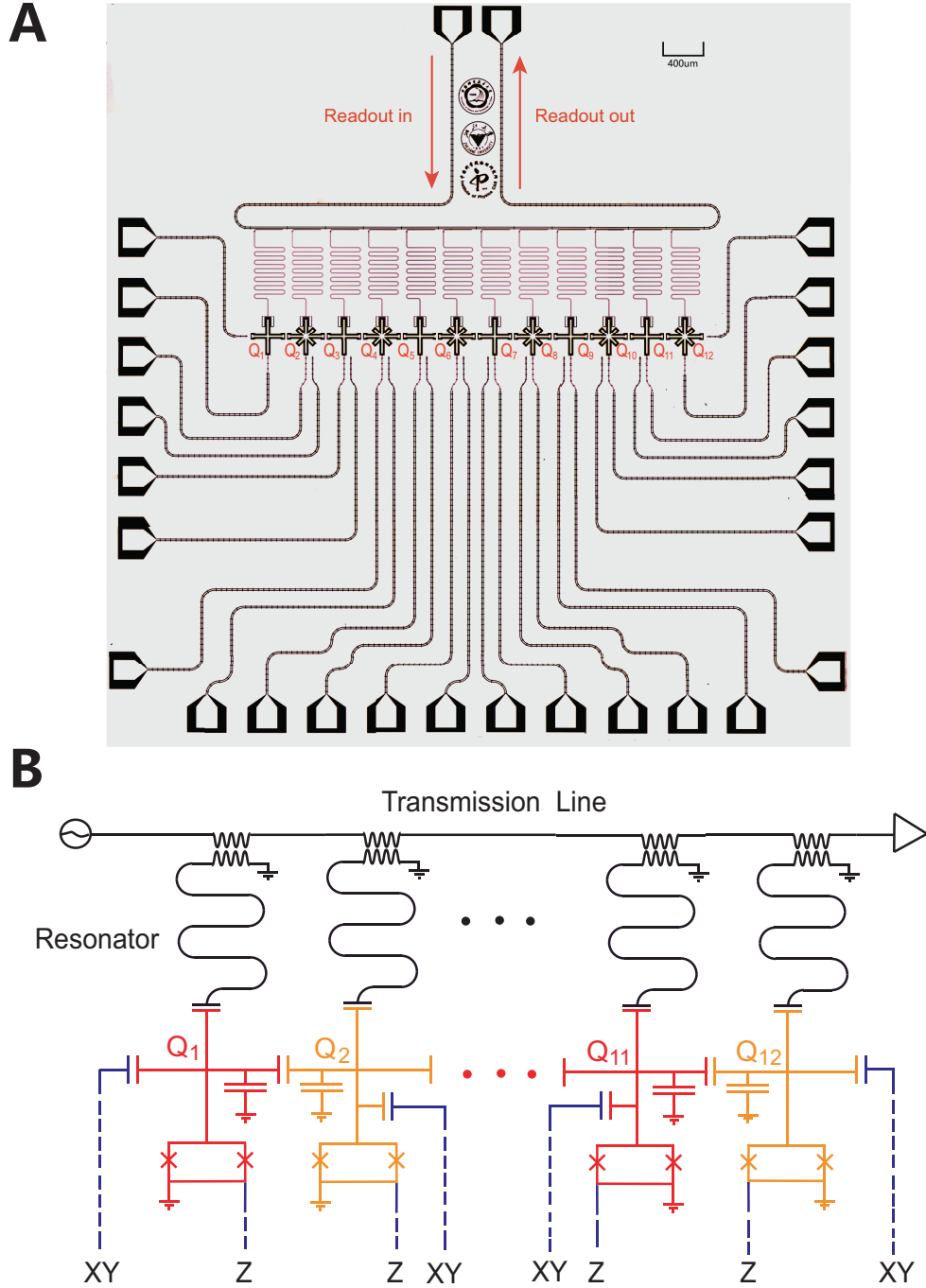


FIG. S1: **(A)** Optical micrograph of the twelve-qubit sample. Each qubit has an independent microwave line for the XY control and a flux bias line for the Z control. Each qubit couples to a separate $\lambda/4$ readout resonator, which couples to the transmission line for simultaneous and individual readout. Crossovers were applied to reduce the impact of the parasitic modes. **(B)** Simplified schematic of the superconducting quantum circuit. The $\lambda/4$ readout resonators inductively couple to the transmission line. The red (yellow) capacitor to ground is C_B , which corresponds to the large shunted capacitor formed by the cross and the ground to suppress the charge noise in each qubit.

coupling strength is determined as $J_{i,j} = 2\pi/2T_{i,j}^{\text{vR}}$, where $T_{i,j}^{\text{vR}}$ is the period of vacuum Rabi oscillations with qubits Q_i and Q_j being in resonance.

For the superconducting qubits used in our experiments, the nonlinear on-site interaction U is equal to the anharmonicity η of the qubit and approximately equals the minus charging energy $-E^C$ [22]. The anharmonicity varies very little with the change of the qubit's frequency. Let us take Q_1 as an example. In our experiments, the measured anharmonicity η_1 changes from -242 MHz to -247 MHz when f_{01} is biased from 5.403 GHz to 4.88 GHz, only giving a very small difference of 2.1% in η_1 . This is also in accordance with our theoretically simulated results. Then, it is found that the dimensionless ratio U/J varies very little when changing the qubit's frequency.

B. Fabrication

The experimental device is fabricated with the following steps:

- (1) A 100 nm aluminum film is deposited directly onto a degassed 2 inch c-plane sapphire wafer in Plassys MEB 550SL3.
- (2) The photo-lithography followed by an evaporation of gold is applied to create alignment marks for the subsequent lithography steps.
- (3) Wet etching is used after photo-lithography by laser direct writing to define the transmission line, control lines, readout resonators, and large pads of the superconducting qubits.
- (4) Electron-beam lithography followed by thermal evaporation of 300 nm GaF_2 film is used to define insulation layer of the crossover.
- (5) The upper electrodes of the crossover are fabricated with electron-beam lithography and evaporation of 300 nm aluminum in Plassys MEB 550SL3.
- (6) The wafer is diced into 9 mm by 9 mm chips.
- (7) The electron-beam lithography, followed by double-angle evaporations of aluminum in Plassys MEB 550SL3, is used to fabricate the $\text{Al}/\text{Al}_2\text{O}_3/\text{Al}$ Josephson junctions.
- (8) The selected chip is wire bonded in an aluminum sample box after transmission line, and all control lines are checked .

C. Experimental wiring set-up

The entire experimental wiring set-up, as illustrated in Fig. S2, consists of three parts, which are: (i) at room temperature, (ii) in the dilution refrigerator (DR), and (iii) under the mixing chamber (MC) plate.

We use 38 Digital-to-Analog Converter (DAC) channels, 2 Analog-to-Digital Converter (ADC) channels, 13 DC channels, and 4 microwave (MW) channels to fully control all 12 qubits. To be more specific, for each qubit, we use two DAC channels connected to an IQ mixer to generate the modulation signal for the XY control, one DAC channel to perform the Z pulse control and one DC channel to DC bias the qubit to its idle point. For the XY control, the qubits on the odd sites share one MW channel and the ones on the even sites share another one. For the readout, we use two

DAC channels and two ADC channels to perform the multi-tone demodulation with frequency-domain multiplexing. One MW channel is used for the signal readout. A room temperature amplifier with over 75 dB gain is used to amplify the readout signal after it gets out of the DR. For the JPA operation, we use one MW channel together with one DAC channel connected to a mixer for gated JPA pumping. One DC channel is used to bias the JPA flux line. Note that there is no Z pulse control line, but only a DC bias line for Q_{12} , due to the shortage of coaxial cables in the DR, so Q_{12} can only be DC biased at a certain idle point but cannot perform fast detuning. All DACs, ADCs and DC sources are customized.

In the DR, the total attenuations for the input of readout signal, XY control and Z control line are 50 dB, 50 dB, and 30 dB, respectively. The attenuators are installed on the still plate and the MC plate to reduce the thermal noise from the higher-temperature plates. For DC control lines, we use RC filters with a 10 KHz cut-off frequency to reduce the high-frequency noise. We install a low-noise high-electron-mobility transistor (HEMT) at the 4K plate for amplifying the readout signal.

Under the MC plate, to reduce high-frequency noise, we use 8 GHz low-pass filters on all XY, Z and readout lines. For Z pulse controls and DC controls, we use 500 MHz and 80 MHz low-pass filters, respectively, to further reduce the high-frequency noise. The Z pulse controls and DC controls are combined together by bias-tees, and then connected to the Z control lines of the quantum device. For the output of the readout signal, we use three circulators to allow the propagation of microwave signal in one direction. On the second circulator, a JPA is used to amplify the signal, which is connected to a bias-tee combining the DC control and microwave pumping signal. The quantum device is placed in a two-layer μ -metal magnetic shield to prevent flux fluctuations induced by the low-frequency vibrations of the system.

D. Qubit Readout

In our experiments, we use two DAC channels and one MW source to generate a multi-tone readout pulse achieved by sideband mixing. The readout signal is pre-amplified by a Josephson Parametric Amplifier (JPA) installed under the MC plate. The design and fabrication details of the Klopfenstein taper JPA can be found in Ref. [25]. In practice, we use one DC channel to bias the JPA and one MW channel to generate a pumping signal. The pumping frequency is about twice of the readout resonator's. The JPA can be switched on and off by turning on and off the MW pumping. In our experiments, we optimize the best working parameters, including the bias amplitude, the pumping frequency and the pumping power, by maximizing the minimum gain at the 12 tones of the resonators. The optimization is realized by using the Nelder-Mead algorithm. A minimum gain of 11.3 dB among all 12 tones is achieved after the optimization, as shown in Fig. S3(A). After the amplification with JPA, the readout signal is then amplified by a HEMT located in the 4K plate, and then further amplified by a room-temperature amplifier after getting out of the DR. The readout signal is then down-converted into two signals and captured by two ADC channels. The signals are converted to digital data by ADC and stored in the Block-RAM of the FPGA. Then, the stored data symbolizing the down-converter IF (intermediate frequency) signals are processed in pipeline and then return the pairs of I and Q values to the PC host through a Gigabit network. For each tone, a pair of I and Q values are returned. The ADC supports the simultaneous processing of 12 frequency points. As an example, the I - Q data for single-shot qubit-state differentiation of Q_7 are presented in Fig. S3(B). The center of the state $|0\rangle$ ($|1\rangle$) is then defined as the mean value of all corresponding data of the state $|0\rangle$ ($|1\rangle$) on the I - Q plot. The distribution histogram along the axis defined by the centers of $|0\rangle$ and $|1\rangle$ states is also shown.

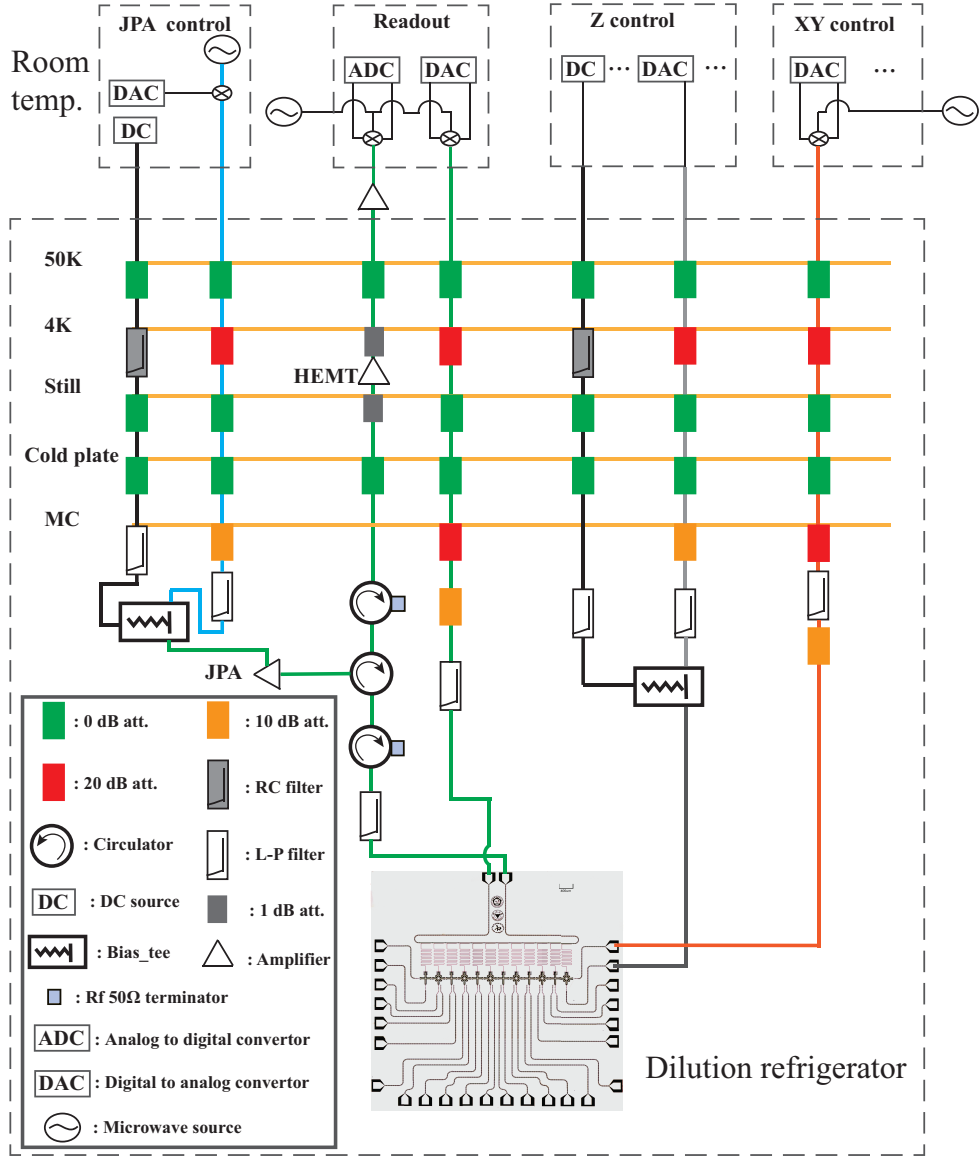


FIG. S2: Overview of the experimental setup. On the top, from left to right, we show the electronics used in the JPA control, readout, qubit Z control, and the qubit XY control, respectively. In the readout box, the DAC and the microwave source generate a twelve-tone microwave pulse targeting all qubits' readout frequencies. Through the transmission line, the readout signal is amplified first by the JPA at the MC plate, then by a HEMT at the 4K plate, and finally by the room temperature amplifier. In the Z control box, each DC source provides a static offset of the qubit frequency by offering a static flux in the DC SQUID loop of the qubit, and each DAC enables a fast detuning of the qubit frequency. In the XY control box, the DAC and the nearby microwave source generate the microwave pulses for the XY control of the qubit. Attenuators and filters are added to all control lines to prevent unwanted noise from disturbing the operation of the qubit device.

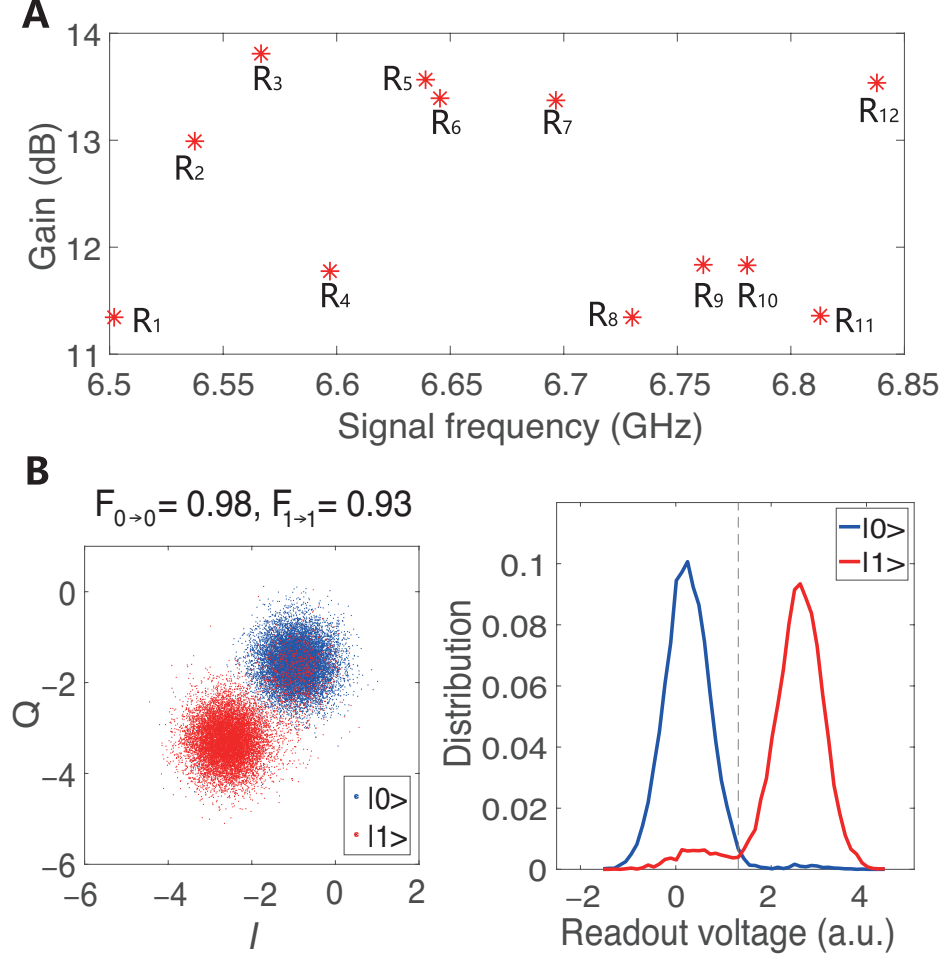


FIG. S3: (A) Gain of the JPA at the frequencies of the readout resonators. R_j represents the readout resonator for Q_j . The gain ranges from 11.34 dB to 13.81 dB (12.51 dB on average). (B) I - Q plot of the signal-shot measurements of Q_7 (left) and the corresponding histograms (right). The total repeat count for each measurement is 12,000. In the histograms, the blue curve is for $|0\rangle$ and the red curve is for $|1\rangle$.

From the data, f_{00}^j and f_{11}^j , which are defined as the probabilities of correct readout of the qubit state after being well-initialized in the $|0\rangle$ and $|1\rangle$ on the j -th qubit, are determined. The readout transition matrix is then obtained by

$$T_n = \begin{pmatrix} f_{00}^j & 1 - f_{11}^j \\ 1 - f_{00}^j & f_{11}^j \end{pmatrix}. \quad (\text{S2})$$

With the transition matrix, the real probability of $|0\rangle$ and $|1\rangle$, which are represented by P_0^r and P_1^r , are corrected as

$$\begin{pmatrix} P_0^r \\ P_1^r \end{pmatrix} = T_n^{-1} \begin{pmatrix} P_0^d \\ P_1^d \end{pmatrix}, \quad (\text{S3})$$

where P_0^d and P_1^d are the measured probability of $|0\rangle$ and $|1\rangle$, respectively. For more than one qubit, the multi-qubit transition matrix is then given by

$$T_{n,m} = T_n \otimes T_{n+1} \cdots \otimes T_m, \quad (\text{S4})$$

which is used to correct the multi-qubit state probability.

E. Waveform sequences

In our experiments, each qubit (except for Q_{12}) is controlled by two different flux controls for different purposes. One is the Z DC control, which is fixed during the experiments. The other is the Z pulse control, which can be used to perform fast detuning. To perform the experiments, the qubits are first DC biased at their idle points. Then, the Z pulse controls detune the qubits to the working point for the state evolution and finally back to the idle points rapidly for the state readout.

To be more specific, the implementation of the experiments consists of four parts: system initialization, state preparation, free evolution, and readout. In the system initialization, we wait for $400 \mu\text{s}$ to cool down all qubits to their ground state $|0\rangle$. Then, in the state preparation, we use the single qubit gate X_j to excite the j -th qubit to its first excited state $|1\rangle_j$. During the system initialization and the state preparation process, the qubits are biased to their idle points by their Z DC control lines to avoid unnecessary XY crosstalk. In the state's free evolution, we detune the corresponding qubits to the working point rapidly and idle for a certain time t . After that, we detune these qubits back to their idle points for the state readout. In the state readout, we have two individual readout methods to obtain the information of the state. The first one is to perform projective measurements to obtain the $\hat{\sigma}_z$ components of the states, and the second one is to perform quantum state tomography (QST) to obtain the density matrix of each qubit. For both methods, we can perform the measurements simultaneously on all qubits.

The idle points are chosen based on the following principles. (i) These idle points should be different from each other to avoid any XY crosstalk. (ii) The unwanted two-level systems coupled to the qubits should be avoided. (iii) The qubits should be as close to their symmetric points as possible to achieve a relatively longer dephasing time. (iv) The f_{12} and f_{01} of different qubits should also not exactly matching, to prevent the XY crosstalk-induced state leakage to their second excited state.

The choice of the working point is much simpler. The only requirement is that there should not be any obvious two-level systems coupled to the qubits. Note that, because of the lack of the Z pulse control line of Q_{12} , it cannot be fast detuned. Thus, in the one-photon experiments, Q_{12} is DC biased away from the working point. In the two-photon experiments, Q_{12} is DC biased to the working point and other qubits are fast detuned to the working point for the system's free evolution.

An example of the waveform sequences for the Fig. 4(A) in main text, i.e., the two-photon experiments, is shown in Fig. S4. Before the waveform sequences, the qubits have been cooled down for $400 \mu\text{s}$. Then, two Gaussian-enveloped sinusoidal pulses, which are used to generate Gaussian-enveloped microwave pulses with the IQ mixers, are applied on Q_6 and Q_7 simultaneously. Each pulse behaves as an $X/2$ gate, and we use two of them combined together to build the X gate. After that, all qubits are detuned to the working point for the system's free evolution. The waveforms to detune the qubits are not simple square Z pulses, resulting from the correction of pulse distortion. Based on our careful correction, each Z pulse is re-modulated so that the qubits can be exactly in resonance when they are tuned together. Details about the pulse distortion calibration can be found in the following sections. We measure the state of the qubits after tuning the qubits back to their idle points.

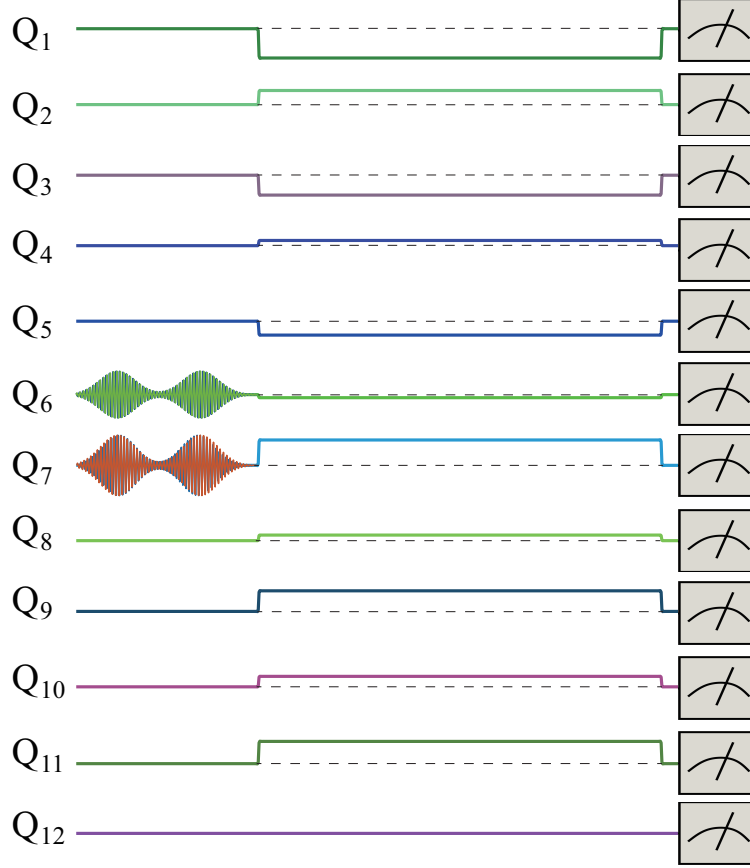


FIG. S4: Experimental waveform sequences for the twelve-qubit two-photon experiments (Q₆ and Q₇ are excited). At first, all the qubits stay at their idle points, while Q₆ and Q₇ are excited by the X gates (two Gaussian-enveloped microwave pulses). Then, all qubits are biased to the working point through their Z pulse control lines. The photons (quasi-particles of the excitations of the qubits) will propagate in the 1D lattice arrays of 12 qubits. After a delay time t , we turn off the Z pulse controls to rapidly tune these qubits back to their idle points, and then measure the state.

II. CALIBRATION

A. Z pulse distortion

In our experiments, we need to tune the qubit frequency by applying the pulse through the Z control line, coupled to the DC-SQUID qubit. Ideally, after applying the Z pulse, we tune the qubit to its idle point for the state readout. However, the unwanted Z pulse distortion causes a frequency drift before the state readout. Such an issue is even worse when we need to measure the $\langle \hat{\sigma}_x \rangle$ component and the $\langle \hat{\sigma}_y \rangle$ component, as the frequency drift causes an apparent phase shift [23]. Therefore, it is necessary to correct the Z pulse distortion.

The pulse sequence we use to measure the Z pulse distortion is shown in Fig. S5(A). Starting with state $|0\rangle$, the qubit is detuned for a given amplitude V_0 for a time longer than $1 \mu\text{s}$. Then, an X/2 microwave pulse is applied after a variable delay time. After waiting for 500 ns for the phase accumulation, we measure the phase of the qubit. The phase response is directly caused by the

pulse distortion, and can be expressed into the form

$$\theta(t) = \sum_i A_i \exp(-B_i t). \quad (\text{S5})$$

Based on this, we extract the frequency drift from the phase response by solving

$$\theta(t_{\text{delay}}) = \sum_i \left[\int_{t_{\text{delay}}}^{t_{X/2}+t_{\text{delay}}} dt \mathbb{F}_i(t) \cdot \text{coff}(B_i) + \int_{t_{X/2}+t_{\text{delay}}}^{t_{X/2}+t_{\text{delay}}+t_{\text{int}}} dt \mathbb{F}_i(t) + \int_{t_{X/2}+t_{\text{delay}}+t_{\text{int}}}^{2 \cdot t_{X/2}+t_{\text{delay}}+t_{\text{int}}} dt \mathbb{F}_i(t) \cdot \text{coff}(B_i) \right], \quad (\text{S6})$$

where t_{int} is 500 ns for the phase accumulation, $t_{X/2}$ is the X/2 gate time, t_{delay} is the delay time before the X/2 gate, and $\text{coff}(B_i)$ is the correction parameter to correct the phase accumulated in the period of the X/2 gate, which is determined from numerical simulations. Here, the frequency drift in the time domain is extracted from the form of

$$\sum_i \mathbb{F}_i(t) = \sum_i a_i \exp(-b_i t). \quad (\text{S7})$$

The relationship between the frequency drift $\sum_i \mathbb{F}_i(t)$ and the fraction of the pulse height, undergoing a distortion $s(t)$, is

$$\sum_i \mathbb{F}_i(t) = s(t) \cdot V_0 \cdot k, \quad (\text{S8})$$

where k is the derivative of the qubit frequency spectroscopy at the idle point, and V_0 is the given pulse amplitude.

With $s(t)$ determined, we can generate a realistic waveform $V_{\text{real}}(t)$ from a given ideal waveform $V_{\text{ideal}}(t)$. In frequency domain, we have $\mathcal{F}(V'_{\text{real}}(t)) = F(\omega)$ and $\mathcal{F}(V'_{\text{ideal}}(t)) = G(\omega)$. Here, there is a transformation given by $F(\omega)[1 - R(\omega)] = G(\omega)$, where $R(\omega)$ is the Fourier transform of $r(t) = s'(t)$. Also, $[1 - R(\omega)]$ is the response function in the frequency domain. Therefore, we have

$$F(\omega) = \frac{G(\omega)}{1 - R(\omega)} = G(\omega)(1 + R + R^2 + R^3 + \dots). \quad (\text{S9})$$

Here, ignoring results greater than third order, as typically $R(\omega) < 0.1$, finally we have

$$V_{\text{real}}(t) = V_{\text{real},0}(t) + V_{\text{real},1}(t) + V_{\text{real},2}(t) + V_{\text{real},3}(t), \quad (\text{S10})$$

$$V_{\text{real},0}(t) = V_{\text{ideal}}(t), \quad (\text{S11})$$

$$V_{\text{real},1}(t) = [V'_{\text{real},0}(t) * s(t)](t), \quad (\text{S12})$$

$$V_{\text{real},2}(t) = [V'_{\text{real},1}(t) * s(t)](t), \quad (\text{S13})$$

$$V_{\text{real},3}(t) = [V'_{\text{real},2}(t) * s(t)](t). \quad (\text{S14})$$

The comparison of the Z Pulse distortion-induced phase accumulation is shown before and after the correction in Fig. S5(B).

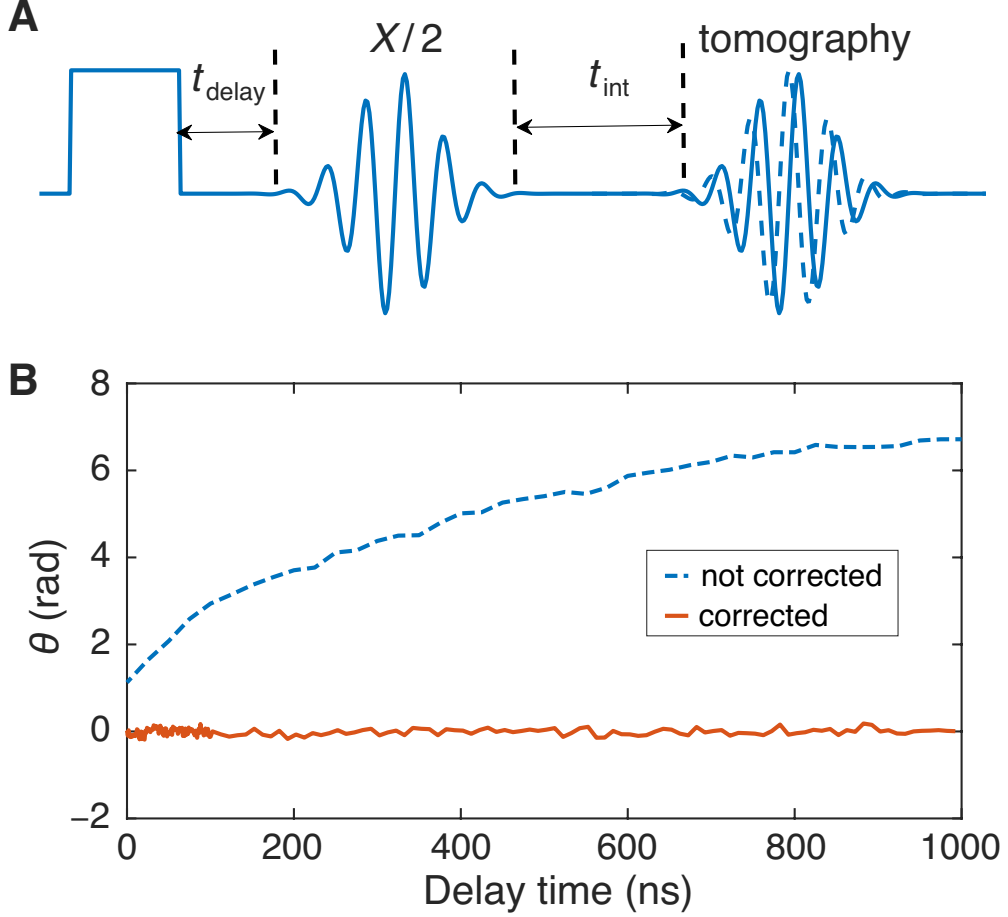


FIG. S5: Correction of pulse distortion. (A) The pulse sequence used to measure the pulse distortion. The $X/2$ pulse is applied with a delay time t_{delay} after the Z pulse. Then, waiting for a time ($t_{\text{int}} = 500$ ns) after the $X/2$ pulse, we measure the qubit's tomography to obtain the accumulated phase. (B) Qubit phase as a function of the delay time t_{delay} . The blue dashed curve and the red solid curve are for qubit phases before and after the correction of pulse distortion, respectively.

B. Z pulse crosstalk correction

In our experiments, we need to bias all qubits to their specific working points by applying Z pulses through Z control lines. Ideally, each Z control line can only bias the corresponding qubit. However, due to unwanted geometric coupling, one Z pulse control line can slightly bias other qubits [23]. Such Z pulse crosstalk can induce frequency drifts, so the qubits cannot be biased to the working point. To correct the crosstalk, we first need to obtain the Z pulse crosstalk matrix.

As illustrated in Fig. S6(A), the procedure we used to measure the crosstalk is to detect the frequency drift of the target qubit when applying the Z pulse on the bias qubit. We apply a square pulse with a fixed length and a variable amplitude on the bias qubit. Then, we measure the transition frequency of the target qubit. We tune the amplitude of the square pulse and obtain the corresponding frequency drift. Then the ratio of the bias qubit frequency drift to the crosstalk of the target qubit Z pulse is obtained. The crosstalk matrix element is defined as the ratio of the bias qubit frequency drift to the crosstalk of the target qubit Z pulse versus that of the bias qubit frequency drift to the Z pulse amplitude of itself. By traversing every related qubit, the crosstalk

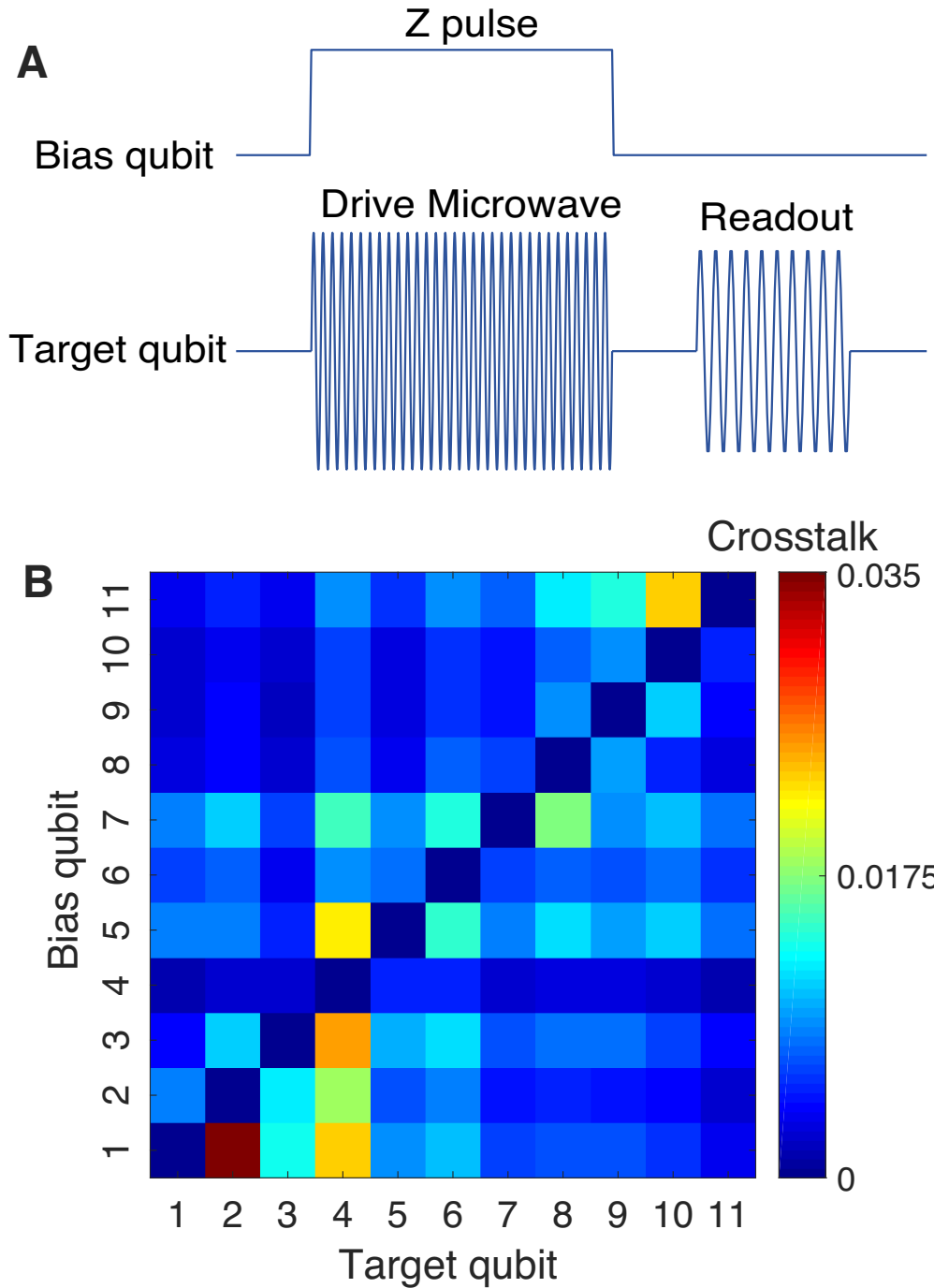


FIG. S6: (A) The procedure to measure the Z pulse crosstalk. The bias qubit's Z pulse and the target qubit's drive pulse are applied in parallel. Then, we measure the state of the target qubit. (B) The measured crosstalk matrix.

matrix is determined.

The measured crosstalk matrix is shown in Fig. S6(B), with element values around 1%~3%. Based on the matrix, we can eliminate the Z pulse crosstalk effect by applying corresponding opposite waveforms. When more than two qubits are involved, the Z control pulse is a linear accumulation of the originally applied waveforms and all related correction waveforms.

C. Single-qubit rotation gate implementation and optimization

In our experiments, the building block for the implementation of single-qubit rotation gates is the X/2 gate, which is realized by generating a Gaussian-enveloped microwave pulse. Two 90 degree shifted Gaussian-enveloped sinusoidal waveforms are generated by two DAC channels and then sent to the I and Q ports of an IQ mixer. The waveforms are defined as

$$I(t) = A \exp[-t^2/(2\sigma_t^2)] \cos(\delta_f t + \varphi_0), \quad (\text{S15})$$

and

$$Q(t) = A \exp[-t^2/(2\sigma_t^2)] \sin(\delta_f t + \varphi_0), \quad (\text{S16})$$

where A controls the amplitude of the microwave pulse, $T_{X/2} = \sigma_t/0.2123$ is the gate length, δ_f is the sideband frequency, and φ_0 is the initial phase. With f_{LO} the frequency of the microwave applied on the LO port of the IQ mixer, the Gaussian-enveloped microwave pulse with frequency $f_{\text{LO}} + \delta_f$ is generated and then sent to the qubit XY control line to drive the qubit.

The transition frequency of the qubit is preliminarily identified by measuring the spectroscopy of the qubit. Then, by combining two X/2 gates to realize the X gate, we measure the Rabi oscillations by adjusting the amplitude to obtain the proper $A_{X/2}$. After that, we correct the qubit frequency by initializing the qubit to its $|+\rangle = (|0\rangle + |1\rangle)/\sqrt{2}$ state and then idle for a series of times t to observe the phase difference in the idling process. The slope of the phase observed corresponds to the difference between the actual qubit frequency and the identified frequency. With the corrected qubit frequency, the X/2 gate amplitude is then corrected by performing the Rabi oscillations again. A derivative reduction by adiabatic gate (DRAG) protocol [24] is used to reduce the phase error. After the DRAG parameter is identified, we correct the gate amplitude $A_{X/2}$ again by applying 25 X pulses to bring the qubit to its $|1\rangle$ state. This operation enlarges the error in the gate amplitude and thus can be used to identify the gate amplitude $A_{X/2}$ with a higher accuracy.

Based on the well-optimized X/2 gate, we generate the Y/2 gate by adding a 90° phase in φ_0 in both $I(t)$ and $Q(t)$. Other elements in the single-qubit Clifford group can be realized by adjusting the initial phase φ_0 or combining these gates together. For a single X/2 (Y/2) gate, the pulse duration is 50 ns. For the X (Y) gate obtained by combining two X/2 (Y/2) gates, the pulse duration is 100 ns.

On this processor, the average single-qubit gate fidelity we determined in the previous experiments is above 0.997, though not at the same idle points in our experiments. With the same optimization process, the gate quality is believed to be on the same level.

III. ADJUSTING ALL QUBITS TO THE SAME FREQUENCY

In our experiments, all qubits need to be detuned to the same frequency. To achieve that, we choose one qubit as a reference and then the working frequencies of the nearest-neighbor coupled qubits by adjusting the corresponding Z pulse amplitudes, as shown in Fig. S7(A). We perform the vacuum Rabi oscillations between the nearest-neighboring qubits to align the nearest-neighboring qubits' frequencies, when one of them is tuned to the working point. To be more specific, let us take the alignment between Q_{10} and Q_{11} as an example. In the measurement of vacuum Rabi oscillations, Q_{11} is first detuned to the working point, previously determined by the frequency alignment with Q_{12} , which is the reference. Then, we sweep the Z pulse amplitude of Q_{10} to

measure the vacuum Rabi oscillations between Q_{10} and Q_{11} . We determine the working point of Q_{10} via the corresponding Z pulse amplitude of Q_{10} , when the vacuum Rabi oscillation period is maximized, as shown in Fig. S7(C). Using this method, we determine the corresponding Z pulse amplitudes to tune all qubits to the same frequency.

With the Z pulse amplitudes of all qubits determined, we can tune all qubits to the working point with the Z crosstalk corrected based on the crosstalk matrix obtained previously, as described in Sec. II B. However, in comparing experimental single-photon quantum-walks results with theoretical predictions, it is found that even though this Z crosstalk correction has been performed, the frequency of the target qubit still shifts when all the Z control pulses are applied synchronously, which indicates the imperfection of the above Z crosstalk correction. To further suppress the crosstalk-induced frequency shift, we perform the *in-situ* Z pulse correction when other qubits' Z pulses are applied. In practice, we measure the qubit's transition frequency when all qubits, except for the corresponding nearest-neighbor two, are tuned to the working point. Subsequently, we obtain the qubit's transition frequency with other qubits' Z pulses being turned off. The *in-situ* Z pulse correction corresponds to the frequency difference under two conditions. Based on the results, as shown in Fig. S7(B), we correct the frequency shift in order to tune all qubits to the working point.

IV. ONE-PHOTON QUANTUM WALKS USING ELEVEN SUPERCONDUCTING QUBITS

In one-photon quantum walks, we only need 11 superconducting qubits to allow a symmetric propagation. To achieve that, we detuned Q_{12} away from the working point of other qubits. By controlling the DC flux applied on the Z control line, we biased the frequency of Q_{12} about 288 MHz lower than the working point to avoid interaction with other qubits, shown in Fig. S7(A). After that, the effective coupling between Q_{11} and Q_{12} is estimated to be $J_{\text{eff}} = J^2/\sqrt{\Delta^2 + J^2} \simeq 2\pi \times 0.533 \text{ MHz} \ll J_{11,12}$, with $J_{11,12}$ being the hopping strength between Q_{11} and Q_{12} , and $\Delta = |\omega_{12} - \omega_{11}|$.

V. THE BOSE-HUBBARD MODEL OF THE NEAREST-NEIGHBOR COUPLED TRANSMON QUBITS

A. Derivation of the Bose-Hubbard model

The effective Hamiltonian of the Cooper-pair box (CPB) system is

$$H^{\text{CPB}} = E^C (\hat{N} - N^g)^2 - E^J \cos \hat{\Phi}, \quad (\text{S17})$$

where \hat{N} and $\hat{\Phi}$ are the number and phase operators of the CPB, respectively, satisfying the commutation relation

$$[\hat{N}, \hat{\Phi}] = -i, \quad (\text{S18})$$

N^g is the induced offset charge on the box controlled by the gate voltage V^g , and E^C and E^J are the charging and Josephson energies, respectively. The transmon qubit is designed to increase the ratio $E^J \gg E^C$ using a large shunt capacitor, whose benefit is its insensitivity to the charge noise, but its disadvantage is a decrease in the anharmonicity. The anharmonicity of the transmon qubit

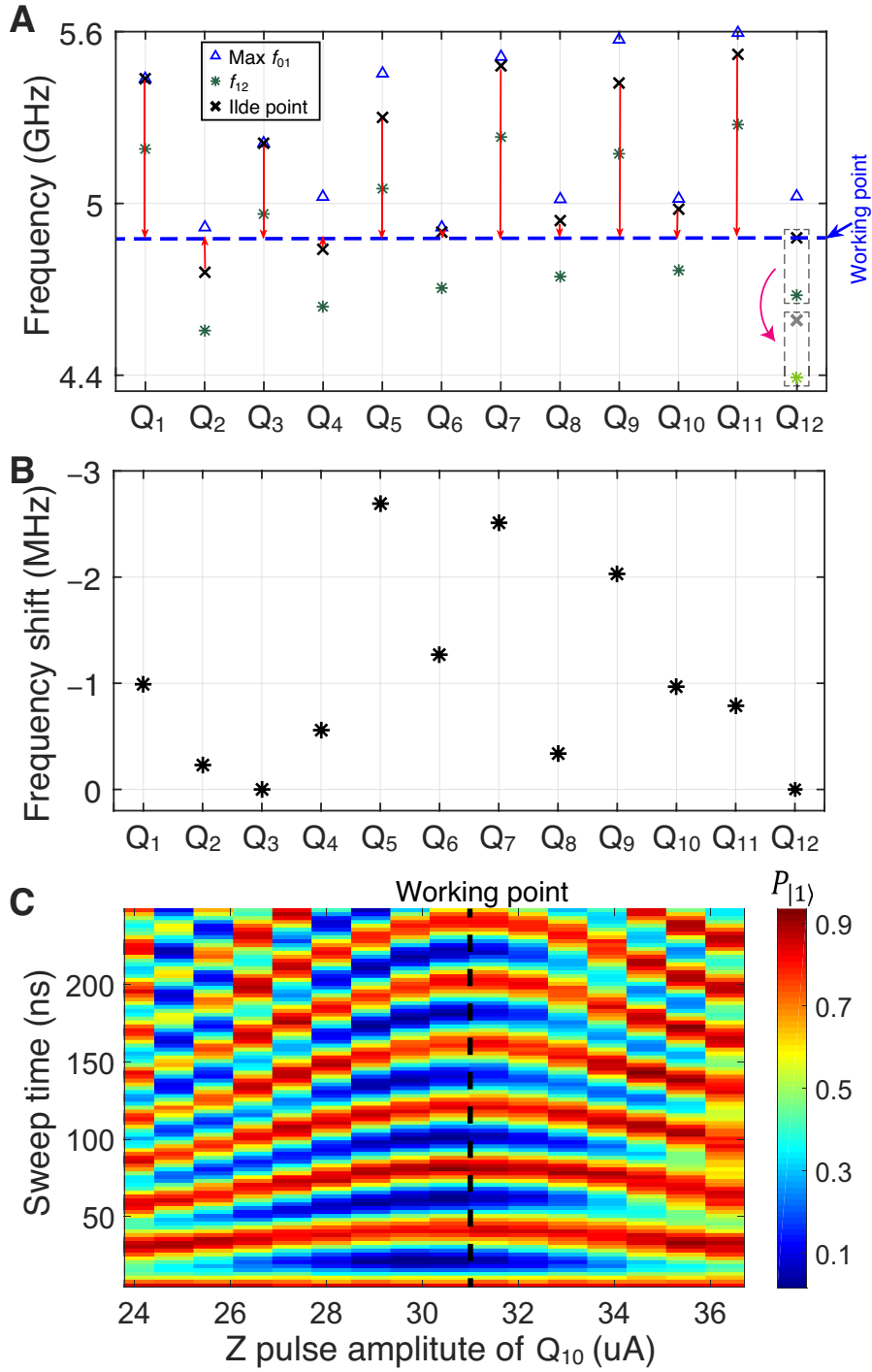


FIG. S7: (A) Qubit frequency diagram. The blue triangle (Δ) represents the maximum frequency $\omega_{\max} = \max\{f_{01}\}$. The black cross (\times) shows the idle frequency ω_{idle} . The blue dashed horizontal line represents the working point. The dark-green asterisk ($*$) represents the energy difference f_{12} between the second excited state and the first excited state, determined at the idle point. In the one-photon quantum walks using 11 qubits, we detune the frequency of the 12-th qubit (Q_{12}) 288 MHz lower than the working point to turn it off. (B) The residual Z crosstalk-induced qubit's frequency shift. (C) Vacuum Rabi oscillations between Q_{10} and Q_{11} used for determining the Z pulse amplitude of Q_{10} , when Q_{11} is detuned to the working point. The dashed line corresponds to the working point of Q_{10} .

is defined as

$$\eta = f_{12} - f_{01}. \quad (\text{S19})$$

Decreased anharmonicity makes it hard to reduce the many-level system of the device to a qubit [22].

In the transmon regime $E^J \gg E^C$, we can neglect the periodic boundary condition of the phase, expand the cosine for small angles up to fourth order, and then rewrite the Hamiltonian in the form of a Duffing oscillator as [22]

$$H^{\text{Tr}} = \sqrt{8E^C E^J}(\hat{n} + 1/2) - \frac{E^C}{12}(\hat{a} + \hat{a}^\dagger)^4 \simeq \sqrt{8E^C E^J}(\hat{n} + 1/2) - \frac{E^C}{2}\hat{n}(\hat{n} + 1) \quad (\text{S20})$$

where $\hat{n} = \hat{a}^\dagger \hat{a}$, with a (a^\dagger) being the bosonic annihilation (creation) operator, the rotating-wave approximation is assumed for the second equality given $E^C \ll E^J$, and N^g can be eliminated by a gauge transformation. We can rewrite the number and phase operators of Cooper pairs in term of the new annihilation and creation operators as

$$\hat{N} = \frac{-i}{2} \left(\frac{E^J}{2E^C} \right)^{\frac{1}{4}} (\hat{a} - \hat{a}^\dagger), \quad \hat{\Phi} = \left(\frac{2E^C}{E^J} \right)^{\frac{1}{4}} (\hat{a} + \hat{a}^\dagger). \quad (\text{S21})$$

As discussed in Ref. [22], the resulting asymptotic expressions for the anharmonicity from numerical simulations is

$$\eta \simeq -E^C. \quad (\text{S22})$$

When considering our sample consisting of 12 coupled transmon qubits, with the nearest-neighbor hopping terms

$$H^I = \sum_{j=1}^{11} J_{j,j+1} (a_j^\dagger a_{j+1} + \text{h.c.}), \quad (\text{S23})$$

the Hamiltonian can be well described by the Bose-Hubbard model as (also used in Ref. [15])

$$H = \sum_{j=1}^{11} J_{j,j+1} (\hat{a}_j^\dagger \hat{a}_{j+1} + \text{h.c.}) + \sum_{j=1}^{12} \frac{U_j}{2} \hat{n}_j (\hat{n}_j - 1) + \sum_{j=1}^{12} h_j \hat{n}_j, \quad (\text{S24})$$

where the nearest-neighbor hopping strength, given in Tab. S1, is measured as $J_{j,j+1} = 2\pi/T_{j,j+1}^{\text{vR}}$, with $T_{j,j+1}^{\text{vR}}$ being the period of vacuum Rabi oscillations when qubits Q_j and Q_{j+1} are in resonance, the on-site nonlinear interaction equals the anharmonicity $U_j \equiv \eta_j \simeq -E_j^C$, and the on-site potential is $h_j = (8E_j^C E_j^J)^{\frac{1}{2}} - E_j^C$. Therefore, each qubit can be regarded as a nonlinear photonic resonator in the microwave regime [15], and our experiments effectively demonstrates quantum walks of interacting microwave photons (quasi-particles of the excitations of the qubits) on a 1D array of transmon qubits (nonlinear photonic resonators).

For single-photon quantum walks, each superconducting qubit can be regarded as a spin- $\frac{1}{2}$ system, and the Bose-Hubbard model reduces to a XX model (the low-filling limit of the Bose-Hubbard model [19])

$$H = \sum_{j=1}^{10} J_{j,j+1} (\hat{\sigma}_j^+ \hat{\sigma}_{j+1}^- + \text{h.c.}) + \sum_{j=1}^{11} h_j \hat{\sigma}_j^- \hat{\sigma}_j^+, \quad (\text{S25})$$

where $\hat{\sigma}_j^+ = |0\rangle_j \langle 1|$, $\hat{\sigma}_j^- = |1\rangle_j \langle 0|$, and the transition frequency of the 12-th qubit (Q_{12}) has been detuned 288 MHz lower than the working point to turn it off.

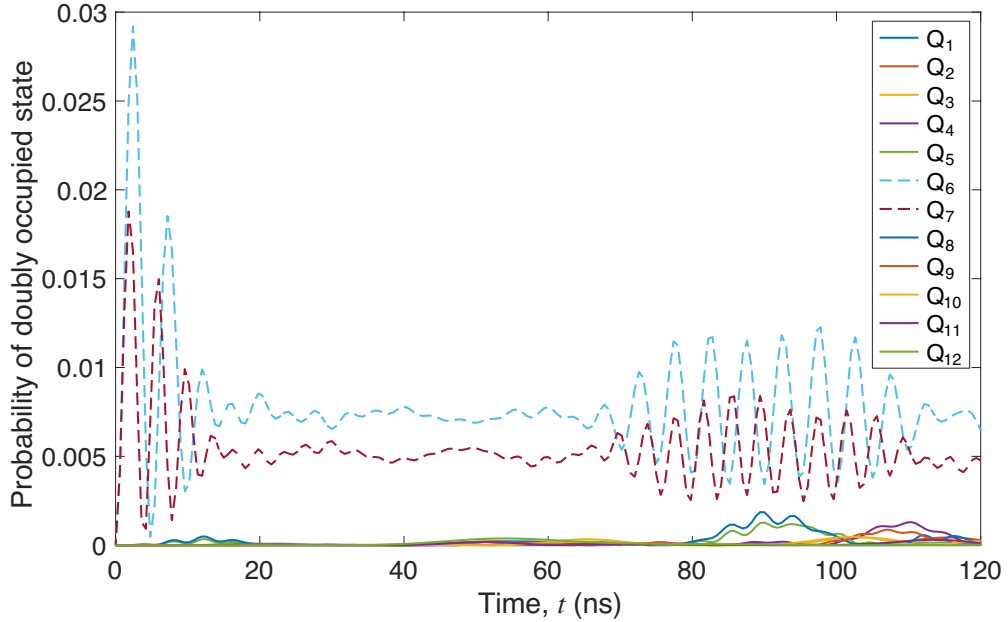


FIG. S8: Numerical results for the probability of the doubly occupied state of each superconducting qubit versus the evolution time for the initial state $\hat{a}_6^\dagger \hat{a}_7^\dagger |0\rangle$.

B. Fermionization of interacting photons

For each transmon qubit, a sufficiently large anharmonicity is required to prevent operations exciting the qubit to a higher energy level [22]. For a 1D array of transmon qubits effectively described by the Bose-Hubbard model (S24), we also need to introduce the dimensionless parameter $u = U/J$ to measure the strength of the on-site nonlinear interaction in units of the hopping strength. In the limit $|u| \rightarrow 0$, the model corresponds to free bosons. However, for $|u| \rightarrow \infty$, the model describes a system of hard-core bosons (a lattice analogue of the Tonks-Girardeau gas), of which the thermodynamics and statistics are identical to free fermions' [19]. In the hard-core limit, the Bose-Hubbard model (S24) can be mapped to the XX model (S25) and solved exactly by the Jordan-Wigner transformation to a system of noninteracting spinless fermions [19]. The fermionization of bosons can be observed by measuring long-range second-order anticorrelations of the Hanbury Brown-Twiss interference during the quantum walks of few particles [30]. For our system, $|u| \simeq 16$ or $20 \gg 1$ and the system is approximately in the hard-core limit. The numerically simulated probability of doubly occupied state against the evolution time given the initial state $\hat{a}_6^\dagger \hat{a}_7^\dagger |0\rangle$ is shown in Fig. S8. The probabilities of the doubly occupied states at all sites are all below 3%, showing that the hard-core limit is a good approximation of our system.

C. The effect of unbalanced qubits' frequencies

Here, we numerically investigate the effect of unbalanced qubits' frequencies on the quantum walks using Eq. (S24) with parameters in Tab. S1. We consider that the on-site potential of each qubit has a disorder $h_j = \bar{h} + \delta h_j$, with $\delta h_j \in [-W/2, W/2]$, and the nearest-neighbor coupling strength can be written as $J_{j,j+1}(\Delta_{j,j+1}) = J_{i,j}^2 / (J_{i,j}^2 + \Delta_{j,j+1}^2)^{\frac{1}{2}}$, with $\Delta_{j,j+1} = h_{j+1} - h_j$ and $J_{j,j+1}$ in Tab. S1.

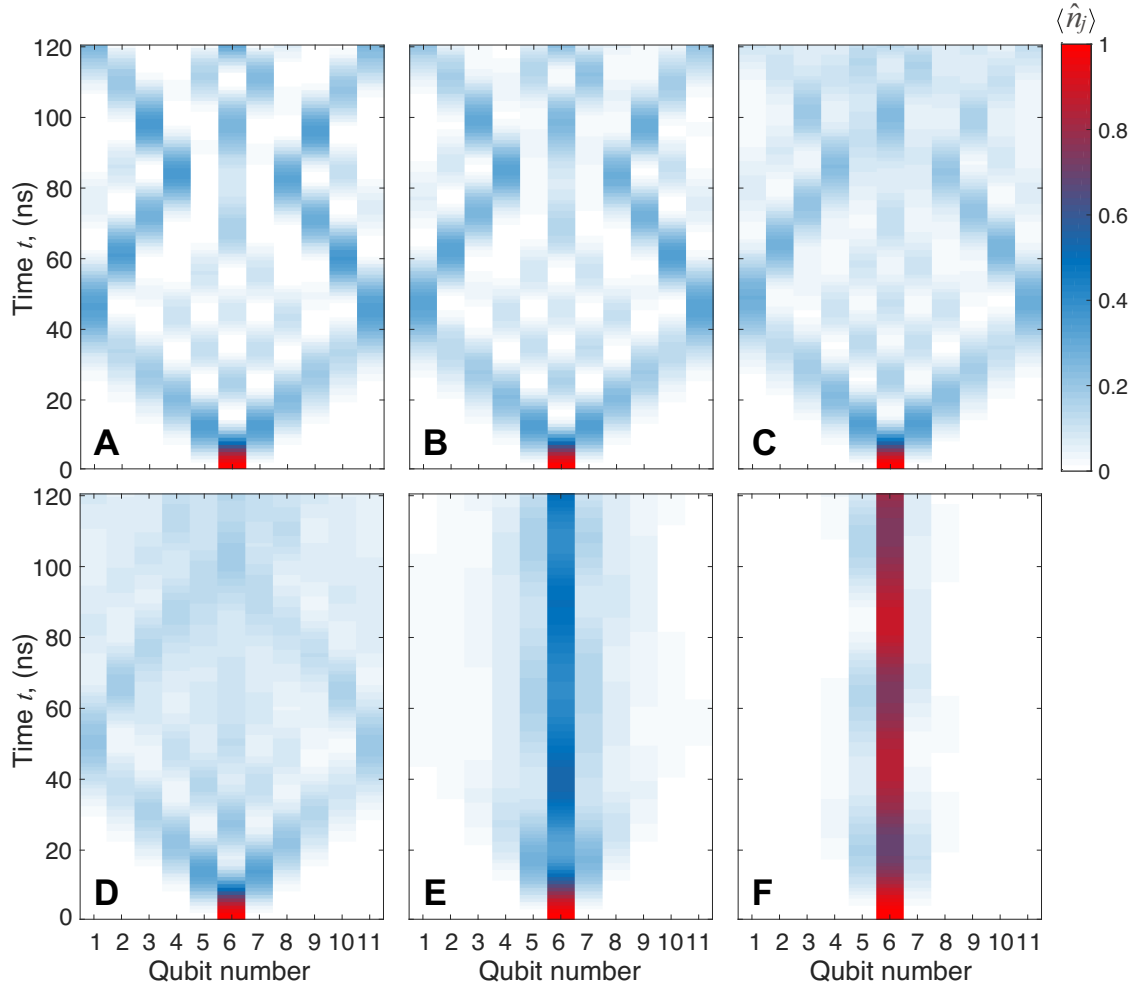


FIG. S9: Density distributions of single-photon experiments versus time, for different strengths of disorder $W/2\pi =$ (A) 0 MHz, (B) 6 MHz, (C) 12 MHz, (D) 20 MHz, (E) 60 MHz, and (F) 200 MHz. The average results are calculated by running 50 sequences.

For the single-photon experiments with the initial state $\hat{a}_6^\dagger|0\rangle$ and a reduced Hamiltonian (S25), the time evolutions of the density distribution for different strengths of disorder $W/2\pi = 0, 6, 12, 20, 60, 200$ MHz are shown in Fig. S9. For the two-photon experiments with the initial state $\hat{a}_6^\dagger\hat{a}_7^\dagger|0\rangle$ and the Bose-Hubbard Hamiltonian (S24), (S25), the time evolutions of the density distribution for different strengths of disorder $W/2\pi = 0, 6, 12, 20, 60, 200$ MHz are shown in Fig. S10. We run 50 sequences of simulations and calculate the average of the density distributions.

In our experiments, the inaccuracy of the frequencies is less than $W/2\pi = 0.5$ MHz. Compared to the numerical simulations shown in Figs. S9(B) and S10(B) with $W/2\pi = 6$ MHz, the unbalanced qubits' frequencies will not affect our experimental results of quantum walks.

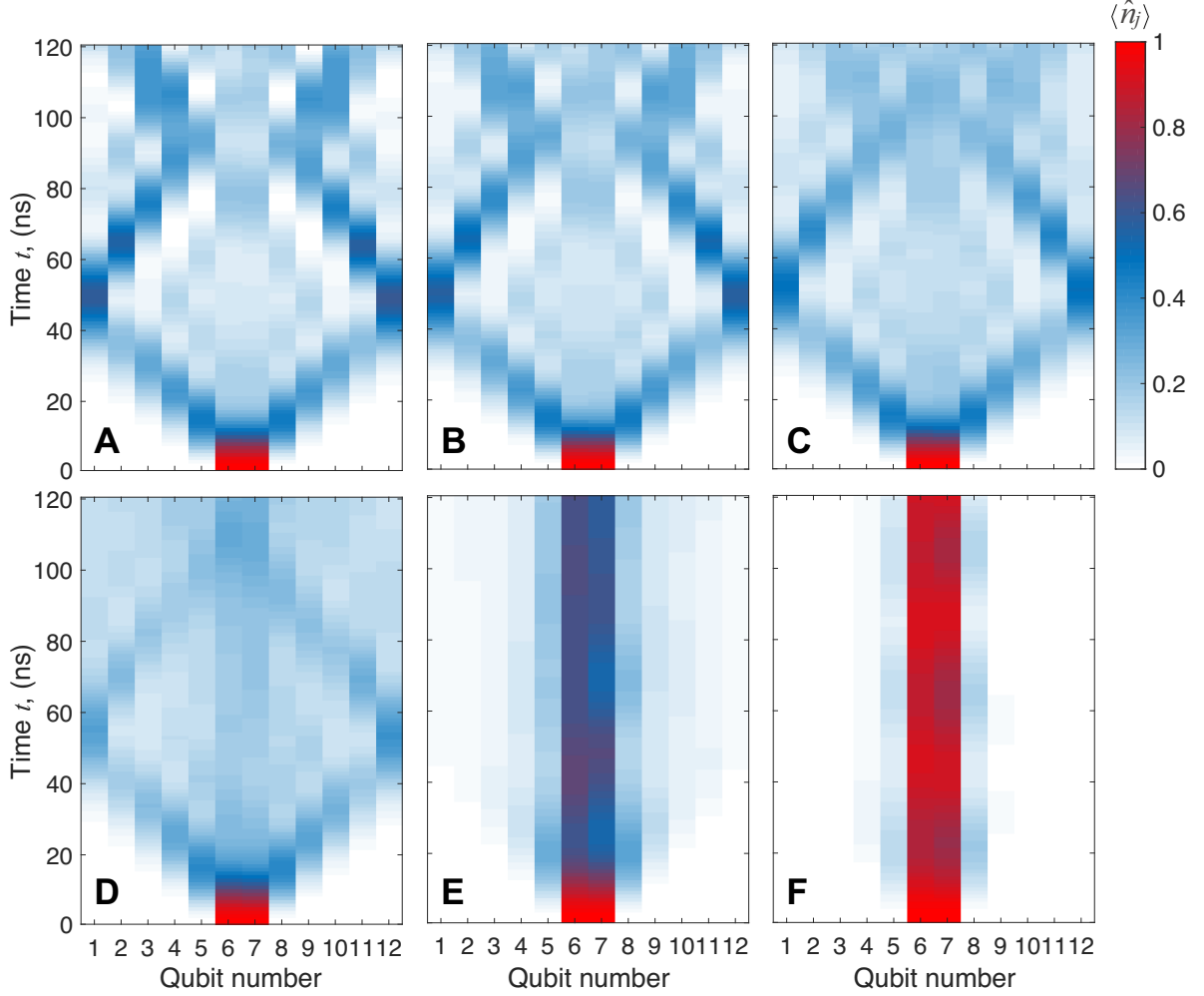


FIG. S10: Density distributions of two-photon experiments versus time for different strengths of disorder $W/2\pi =$ (A) 0 MHz, (B) 6 MHz, (C) 12 MHz, (D) 20 MHz, (E) 60 MHz, and (F) 200 MHz. The average results are calculated by running 50 sequences.

D. Numerical simulations of continuous-time quantum walks

Numerical computations were performed using the QUTIP (the quantum toolbox in PYTHON) and NUMPY. For continuous-time quantum walks with equal on-site potentials of all qubits $h_j = h$, the time evolutions of the system with a Hamiltonian in Eq. (S24) after initial states' preparation were numerically simulated using QUTIP's master equation solver `mesolve`, where the parameters in Tab. S1 were used. We simulated all transmon qubits in the Fock space of cutoff dimensions $D = 2$ (qubit space) and $D = 3$ for single-photon and two-photon quantum walks, respectively. Because the evolution time is much shorter than the qubits' energy relaxation time and dephasing time $t \ll T_1, T_2$, we did not consider the effect of decoherence in simulations.

E. The effect of the measurement precision of the nearest-neighbor coupling strength

For the numerical simulations, we use the coupling strength presented in Tab. S1. In our experiments, the hopping strength is determined by $J_{i,j} = 2\pi/2T_{i,j}^{\text{VR}}$, where $T_{i,j}^{\text{VR}}$ is the period of the vacuum Rabi oscillations with qubits Q_i and Q_j being in resonance. The inaccuracy of the measured nearest-neighbor coupling strength would affect the fidelity $F(t) = \sum_{j=1}^{11} \sqrt{p_j(t)q_j(t)}$, as shown in Fig. 3(A), for the measured and theoretical probability distributions $p_j(t)$ and $q_j(t)$. In Fig. S11, we show the numerical results of the fidelity of the ideal theoretical probability distribution and the one whose coupling strengths have a maximum $\pm 2.5\%$ random error. The numerical results in Fig. S11 agree with the experimental results in Fig. 3(A), which explain the facts that (i) the fidelity has a fluctuation during the evolution, and (ii) the fidelity starting from the central-localized state decays faster than the ones starting from the leftmost- and rightmost-localized states, as a result of the inaccuracy in the determined coupling strengths. The numerical results, will be slightly changed, if we consider the decoherence of each qubit (using QUTIP with decoherence time given in Tab. S1) and the unbalanced qubits frequencies (with random disorder of the width 0.5 MHz), which are not the main reasons for the large fluctuation and decay of the fidelity from the central-localized state.

We note that the fidelity $F(t)$ of the distribution of the evolved state and the one given by numerical simulations will vary a lot from the distributions. For example, with the same noise, the evolved state with a highly concentrated distribution (e.g., a single localized excitation) would have a larger fidelity than a superposed state with a uniform distribution which is more fragile to the noise. The fidelity starting from the central-localized state would decay faster than the ones starting from the leftmost- and rightmost-localized states, because the state from the central-excited qubit performs the propagation of large coherence and entanglement propagation, of which the fidelity is more sensitive to the inaccuracy of the measured nearest-neighbor coupling strengths. The large fluctuations of the fidelity $F(t)$ mainly arise from the inaccuracy of the measured nearest-neighbor coupling strengths, according to our numerical results in Fig. S11.

VI. LIEB-ROBINSON BOUND

The Lieb-Robinson bound is a theoretical upper limit on the speed at which information can propagate in non-relativistic quantum systems. For the one-photon quantum walks with system initialized at $|\psi_0\rangle = |\mathbf{0}\rangle = \bigotimes_{j=1}^{11} |0\rangle_j$, and then prepared at $|\psi_{t=0}\rangle = \hat{\sigma}_i^x |\psi_0\rangle$, we consider the change of the number operator at site j , $\hat{n}_j = (\mathbb{I} - \hat{\sigma}_j^z)/2$, which can be bounded by [29]

$$|\langle \psi(t) | \hat{n}_j | \psi(t) \rangle - \langle \psi_0 | \hat{n}_j | \psi_0 \rangle| \leq \| [U^\dagger(t) \hat{n}_j U(t), \hat{\sigma}_i^x] \| \quad (\text{S26})$$

$$= \frac{1}{2} \| [U^\dagger(t) \hat{\sigma}_j^z U(t), \hat{\sigma}_i^x] \| \leq c \exp\left(\frac{d - v|t|}{\xi}\right) \quad (\text{S27})$$

where $d = |i - j|$ is the distance, $U(t) \equiv \exp(-iHt)$ is the time evolution operator. Here, c , v (the so-called Lieb-Robinson velocity), and ξ are positive constants, which depend on the interactions and lattice structure. The Lieb-Robinson bound (S27) shows that the amount of information outside the light cone is exponentially decaying. For the system with only nearest-neighbor interactions, a tighter bound can be written as [29]

$$\langle \psi(t) | \hat{n}_j | \psi(t) \rangle \leq I_d(4gt) \quad (\text{S28})$$

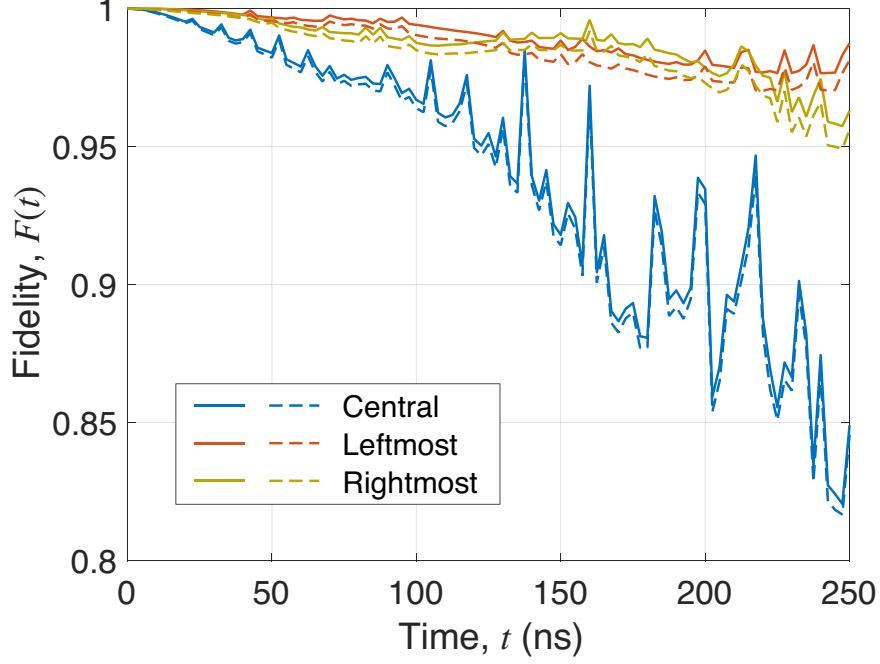


FIG. S11: The blue, red and yellow solid lines are for the numerical results of the fidelities of the ideal theoretical probability distribution and the one of which the measured coupling strength is assumed to have a random error within $\pm 2.5\%$, starting from the central-, leftmost- and rightmost-localized states, respectively, versus the time t . The dashed lines are for the fidelities, when the decoherence of each qubit and the unbalanced qubits frequencies are considered.

where $I_d(x)$ is the modified Bessel function of the first kind, and $g = \max(J_{j,j+1})$.

In Fig. 3C, the shaded regions denote the forbidden areas inside the “light cone”, and the boundaries are predicted by Eq. (S28). Because the signal for each qubit is well outside the corresponding forbidden area, the Lieb-Robinson bound for single-photon quantum walks is verified in our experiments.

The maximal group velocity can be calculated as [18]

$$v_g^{\max} = \left| \frac{\partial \omega}{\partial k} \right| = |(\omega_{k_{n+1}} - \omega_{k_n})(L + 1)/\pi|, \quad (\text{S29})$$

where the wavevector $k_n = n\pi/(L+1)$, with $L = 11$ and $n = 1, 2, \dots, L$, and ω_k is the eigenmode spectrum of the effective Hamiltonian

$$H_{\text{hc}} = \sum_{j=1}^{10} J_{j,j+1} (\hat{a}_j^\dagger \hat{a}_{j+1} + \text{h.c.}) = \sum_k \omega_k \hat{a}_k^\dagger \hat{a}_k. \quad (\text{S30})$$

With the values of $J_{j,j+1}$ given in Tab S1, we can obtain the maximum group velocity as $v_g^{\max} = 153.99$ site/ μs , see Fig. S12, which is larger than the group velocity of the spread of the concurrence, von Neumann entropy, and density distributions, see Fig. S13.

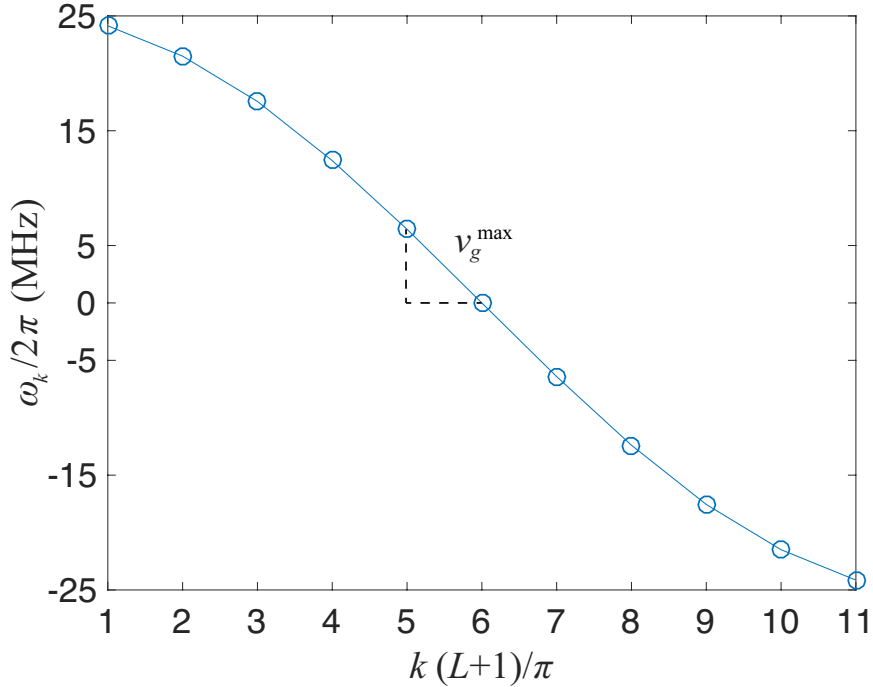


FIG. S12: Dispersion relation numerically predicted using the experimental parameters given in Tab. S1. The maximum group velocity v_g^{\max} is inferred from the steepest slope.

VII. COMPARISON WITH PREVIOUS WORK

A. One-photon quantum walks

Quantum walks of a single particle demonstrate the spreading of quantum information governed by the Lieb-Robinson bounds. In Ref. [26], the propagation of quasiparticle pairs was shown by the two-point parity correlation functions with a chain of atoms. The number of atoms in each chain ranged between 10 and 18. The propagation velocity of correlations across the system was observed to satisfy the “light cones” of the Lieb-Robinson bounds.

Later, the propagation of the quantum nature of correlations such as entanglement was observed in a chain of 7 atomic ions with long-range interactions [18]. The entanglement was shown to propagate from the center to the boundaries of the system. Using non-local correlations, similar work investigating global quenches of trapped-ion chains were done in Ref. [9].

In our experiments, quantum walks of a single particle were implemented in an open chain of 11 superconducting qubits. High fidelity entanglement propagation was observed. Explicitly, we observed not only entanglement propagation from the center to the boundaries, but also the reflected entanglement. In addition to the main wavefronts of the entanglement, the explicit sub-wavefronts of entanglement were also observed. The observation of reflected entanglement highlights the long-coherence time of the superconducting quantum processor. The importance of observation of sub-wavefronts of entanglement lies in the fact that this phenomenon is due to the quantum superposition principle. It does not have classical counterparts.

B. Two-photon quantum walks

Quantum walks of correlated particles implement Hanbury Brown-Twiss interference, and their dynamical behaviors are sensitive to particle statistics. In Ref. [12], the bunching and antibunching effects of bosonic ^{87}Rb atoms with tunable dimensionless repulsive interactions were demonstrated by measuring the density-density correlators in optical lattices, which showed the fermionization of bosons using quantum walks.

In our experiments, we implemented quantum walks of two strongly interacting microwave photons in an array of artificial atoms (a chain of 12 superconducting qubits). We explicitly observed fermionization of strongly interacting bosons, which is identical to the dynamical behavior of noninteracting spinless fermions. Moreover, our one-dimensional systems have strong attractive interactions instead of repulsive ones, so our results also verify that the fermionization of bosons depend on the strength of the interaction, but not on its sign.

VIII. EXTENDED DATA

Extended figures for illustrating approximate linear “light cones” of quantum walks of a photon initially localized at the central qubit (Fig. S13) and comparisons between the experimental results and theoretical predictions of one- and two-photon quantum walks (Fig. S14–S20).

The extended movie shows the time-evolved normalized density-density correlators $\Gamma_{ij}/\Gamma_{ij}^{\max}$ from 2.5 ns to 55.5 ns with two photons initially localized in the central-neighbor qubits Q_6 and Q_7 , respectively (see Movie S1, Fig. S19(A) and Fig. S20(A–F)). The movie exhibits the process of antibunching and fermionization of two photons in a superconducting processor.

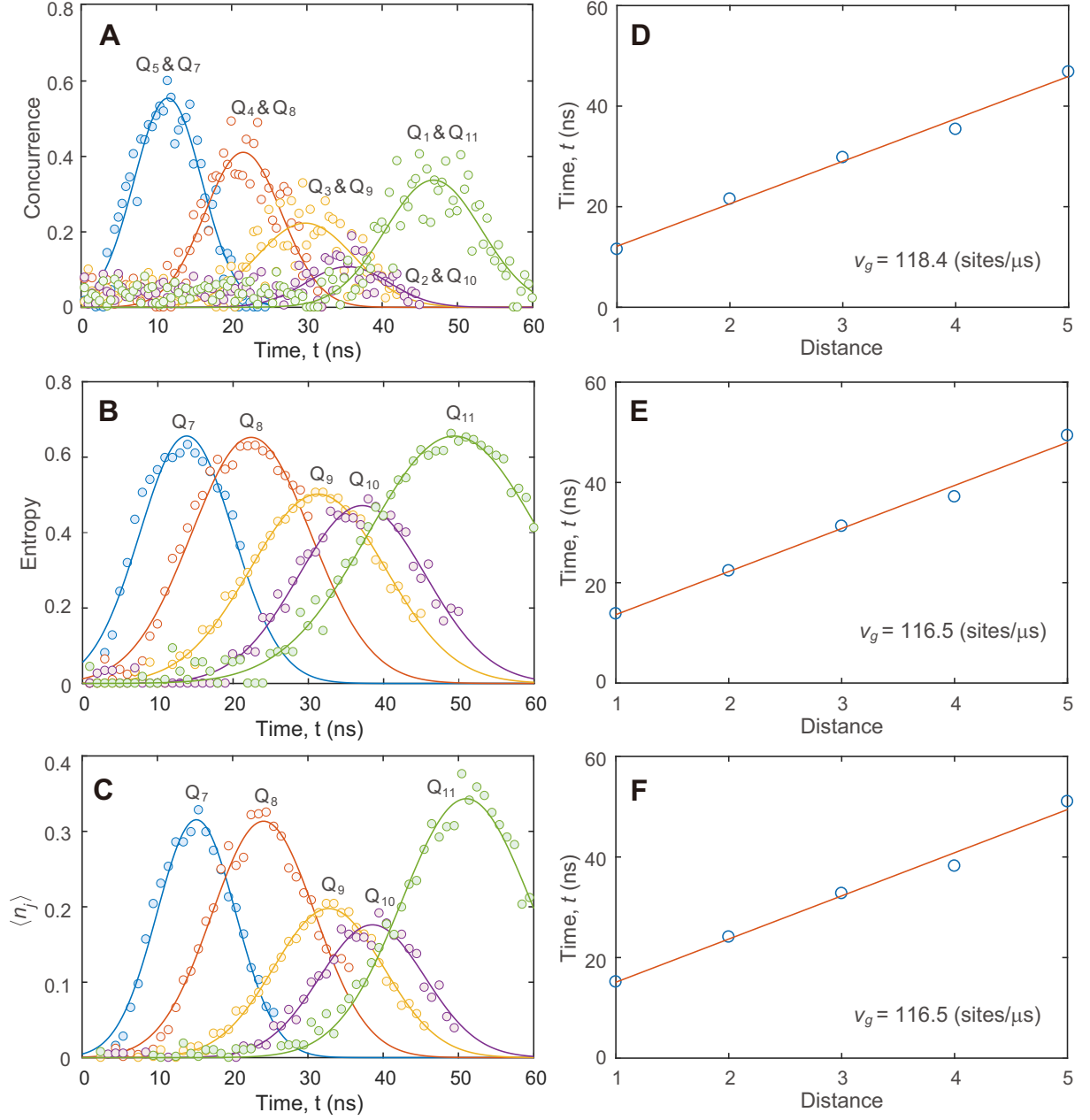


FIG. S13: Approximate linear “light cones” of quantum walks of a photon initially localized at the central qubit. Experimental measurements of the spread of (A) concurrence, (B) von Neumann entropy and (C) density distributions during quantum walks (solid curves are Gaussian fits of the wavefronts). Linear fits of the group velocity of the spread of (D) concurrence, (E) von Neumann entropy and (F) density distributions, yielding several approximate linear “light cones”.

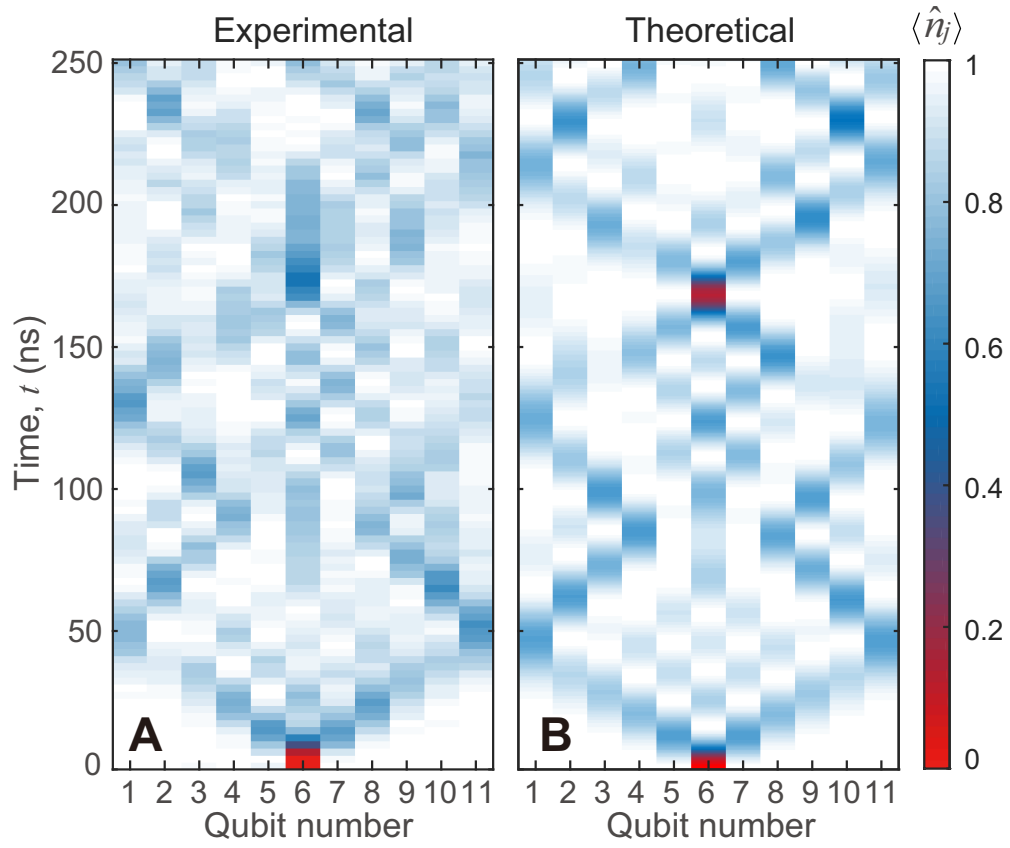


FIG. S14: Comparison of (A) experimental results and (B) theoretical predictions of the time evolution of the density distribution for the single-photon central-localized quench. Namely, the photon is initially localized in the central qubit (Q_6), and then the system evolves in time.

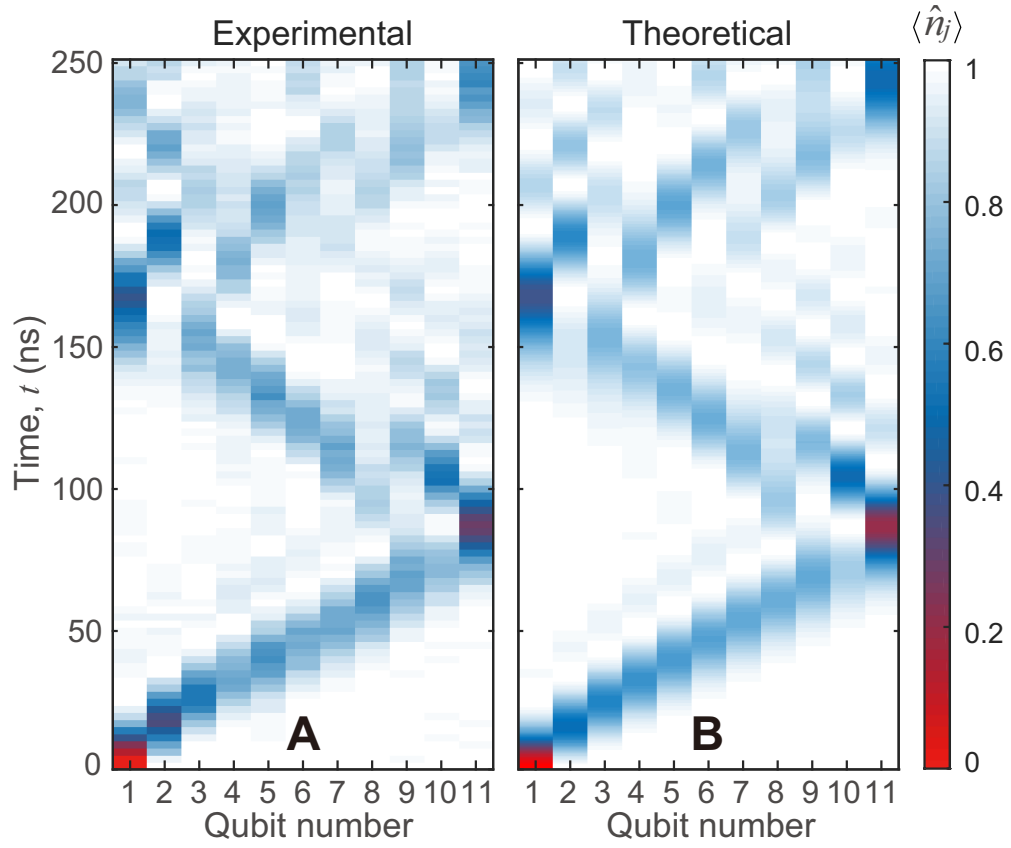


FIG. S15: Comparison of (A) experimental results and (B) theoretical predictions of the time evolution of the density distribution for the single-photon leftmost-localized quench. Namely, the photon is initially localized in the leftmost qubit (Q_1), and then the system evolves in time.

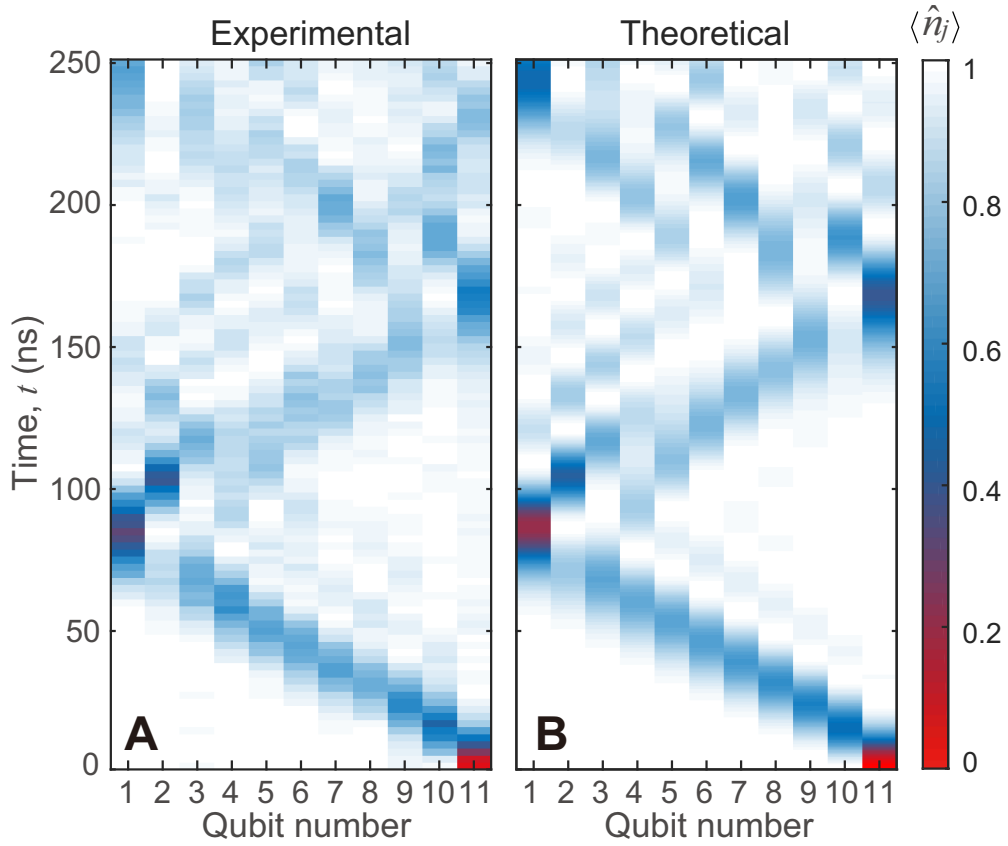


FIG. S16: Comparison of (A) experimental results and (B) theoretical predictions of the time evolution of the density distribution for the single-photon rightmost-localized quench. Namely, the photon is initially localized in the rightmost qubit (Q_{11}), and then the system evolves in time.

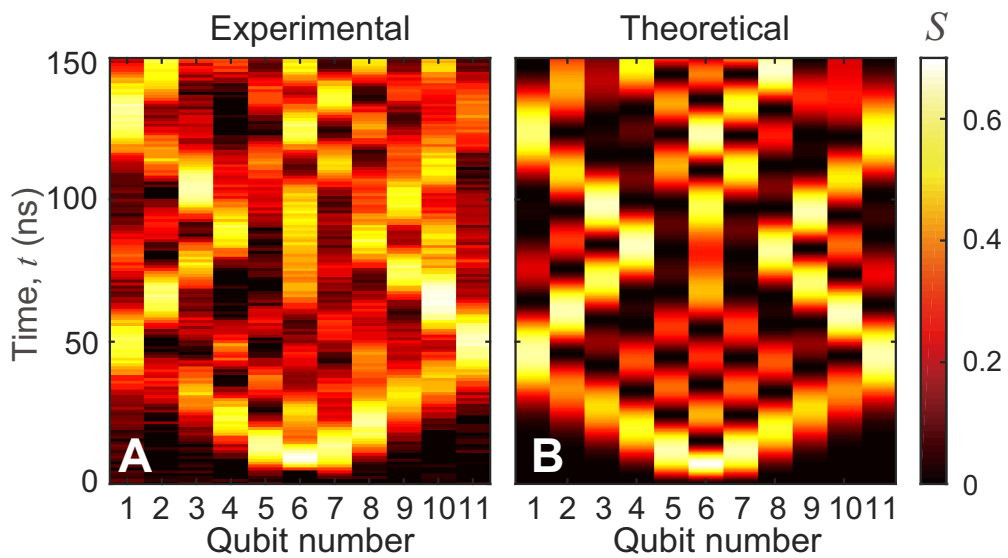


FIG. S17: Comparison of (A) experimental results and (B) theoretical predictions of the time evolution of the von Neumann entropy for the single-photon central-localized quench.

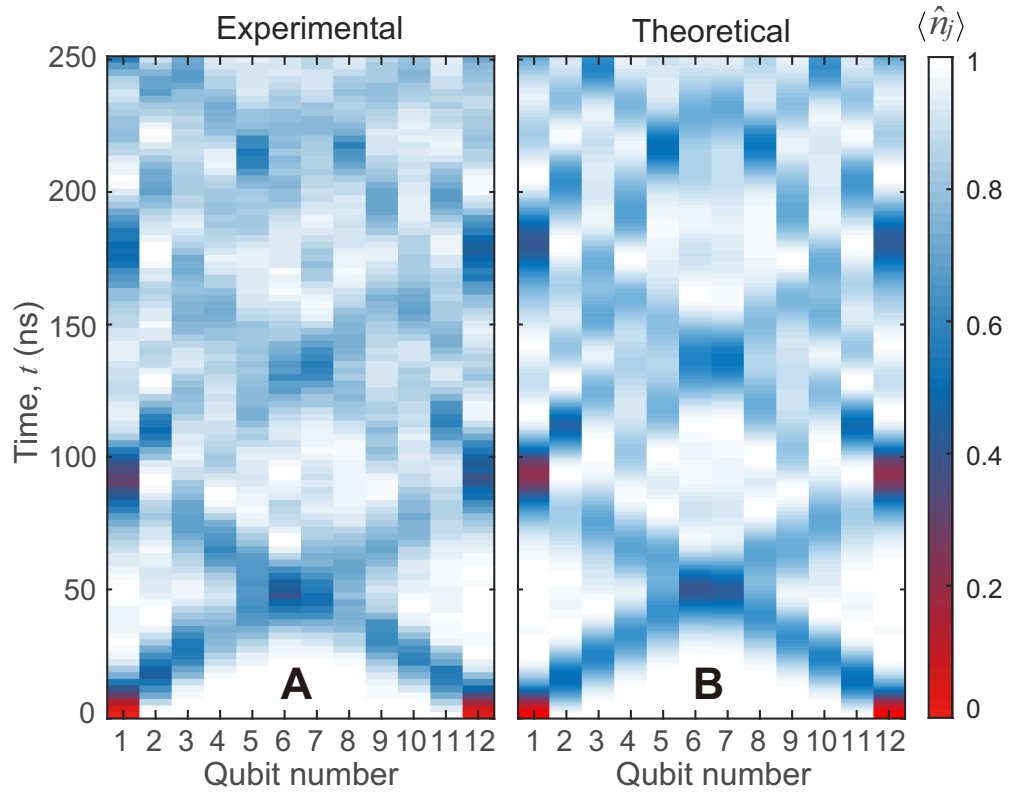


FIG. S18: Comparison of (A) experimental results and (B) theoretical predictions of the time evolution of the density distribution for the two-photon two-boundary-localized quench. Namely, two photons are initially localized in the leftmost qubit (Q_1) and the rightmost qubit (Q_{12}), respectively, and then the system evolves in time.

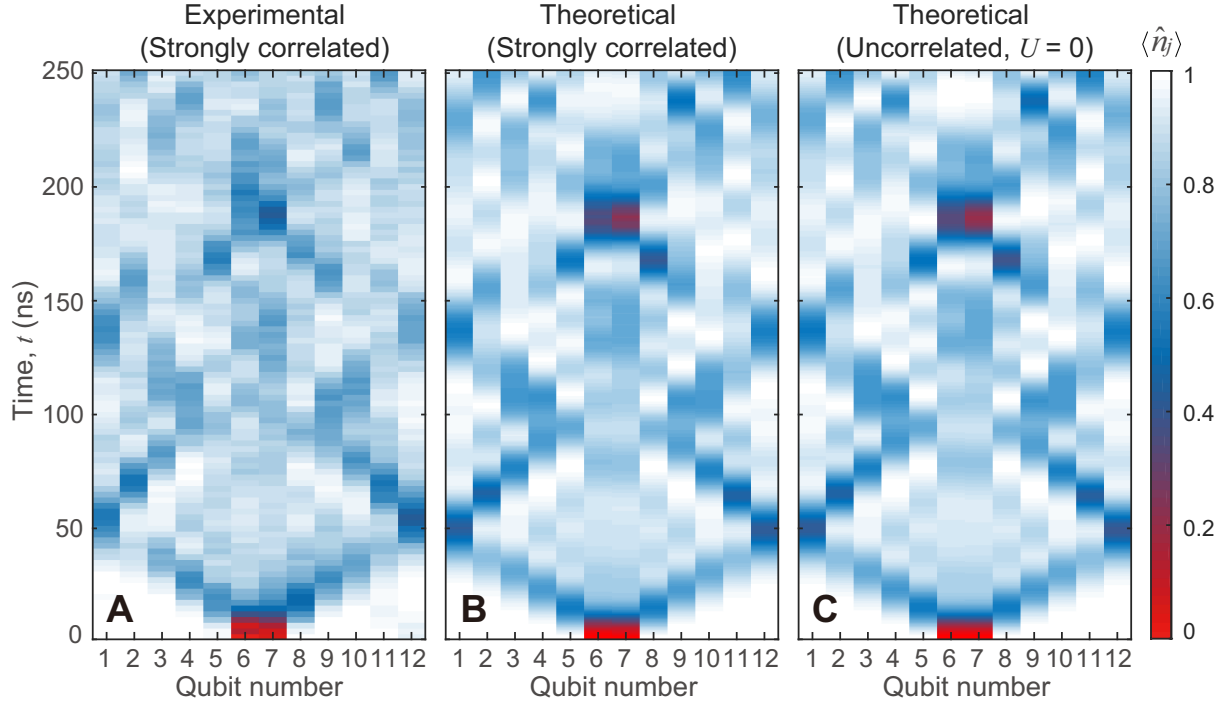


FIG. S19: Comparison of (A) experimental results, (C) theoretical predictions and (B) theoretical predictions of uncorrelated free photons of the time evolution of the density distribution for the two-photon central-neighbor-localized quench. Namely, two photons are initially localized in the central-neighbor qubits Q_6 and Q_7 , respectively, and then the system evolves in time. Note that the time evolutions of the density distributions of the strongly correlated are also similar to those of uncorrelated bosons.

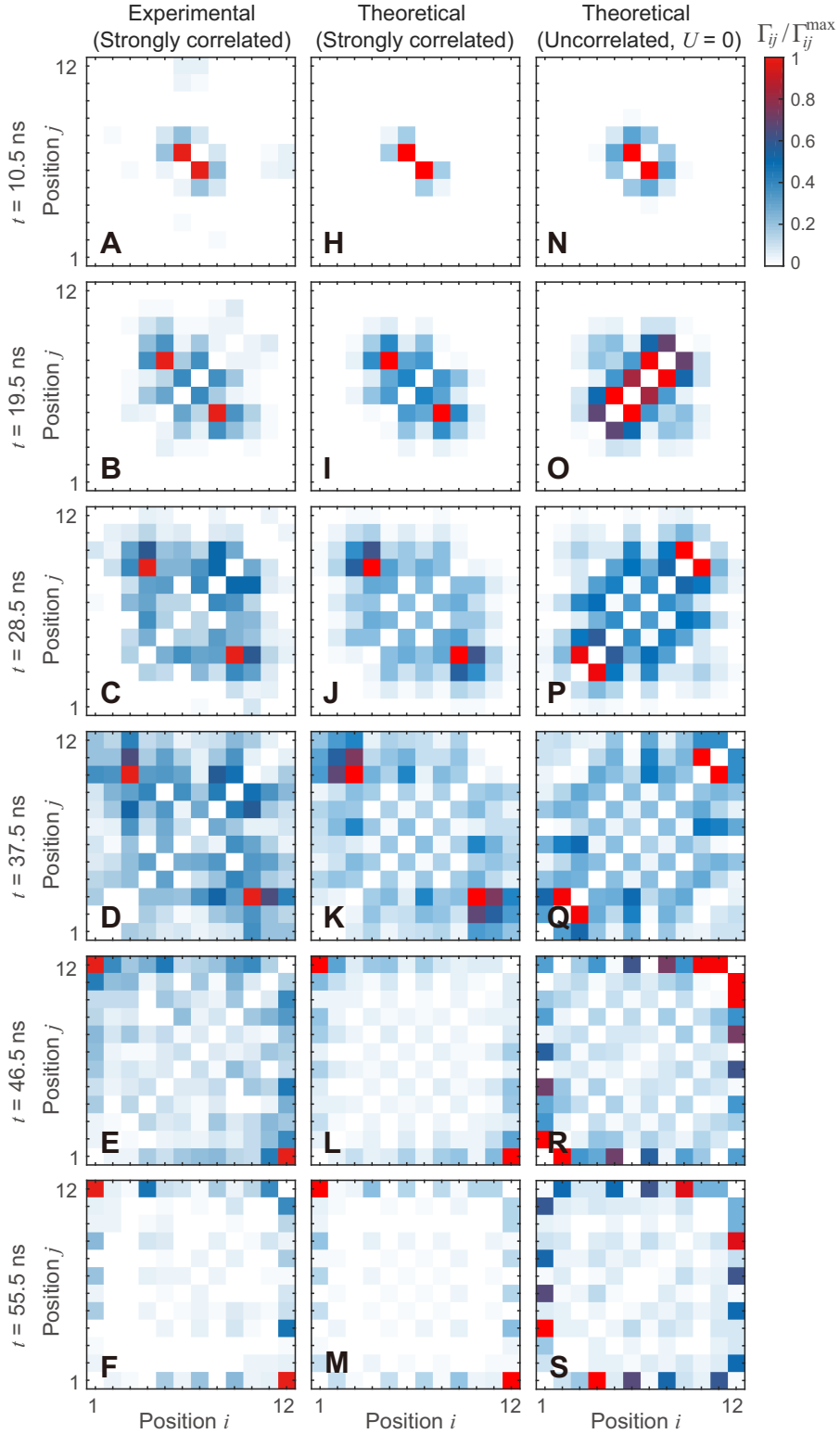


FIG. S20: Comparison of (A–F) experimental results, (H–M) theoretical predictions and (N–S) theoretical predictions of uncorrelated free photons of the time evolution of the normalized density-density correlators $\Gamma_{ij}/\Gamma_{ij}^{\max}$ for the two-photon central-neighbor-localized quench. We clearly observed the anticorrelations demonstrating fermionization, compared to the free bosons cases, where composite probabilities concentrate around the diagonal of the normalized correlator.

Movie S1: The time evolution of the two-site correlators $\Gamma_{ij}/\Gamma_{ij}^{\max}$ measured during the quantum walks of two strongly correlated photons at different evolution times. It shows the process of antibunching and fermionization of two photons in a superconducting processor.

References and Notes

1. Y. Aharonov, L. Davidovich, N. Zagury, Quantum random walks. *Phys. Rev. A* **48**, 1687–1690 (1993). [doi:10.1103/PhysRevA.48.1687](https://doi.org/10.1103/PhysRevA.48.1687) [Medline](#)
2. E. Farhi, S. Gutmann, Quantum computation and decision trees. *Phys. Rev. A* **58**, 915–928 (1998). [doi:10.1103/PhysRevA.58.915](https://doi.org/10.1103/PhysRevA.58.915)
3. I. Buluta, F. Nori, Quantum simulators. *Science* **326**, 108–111 (2009). [doi:10.1126/science.1177838](https://doi.org/10.1126/science.1177838) [Medline](#)
4. A. M. Childs, D. Gosset, Z. Webb, Universal computation by multiparticle quantum walk. *Science* **339**, 791–794 (2013). [doi:10.1126/science.1229957](https://doi.org/10.1126/science.1229957) [Medline](#)
5. B. Do, M. L. Stohler, S. Balasubramanian, D. S. Elliott, C. Eash, E. Fischbach, M. A. Fischbach, A. Mills, B. Zwickl, Experimental realization of a quantum quincunx by use of linear optical elements. *J. Opt. Soc. Am. B* **22**, 499–504 (2005). [doi:10.1364/JOSAB.22.000499](https://doi.org/10.1364/JOSAB.22.000499)
6. A. Peruzzo, M. Lobino, J. C. F. Matthews, N. Matsuda, A. Politi, K. Poulios, X.-Q. Zhou, Y. Lahini, N. Ismail, K. Wörhoff, Y. Bromberg, Y. Silberberg, M. G. Thompson, J. L. O'Brien, Quantum walks of correlated photons. *Science* **329**, 1500–1503 (2010). [doi:10.1126/science.1193515](https://doi.org/10.1126/science.1193515) [Medline](#)
7. C. A. Ryan, M. Laforest, J. C. Boileau, R. Laflamme, Experimental implementation of a discrete-time quantum random walk on an NMR quantum-information processor. *Phys. Rev. A* **72**, 062317 (2005). [doi:10.1103/PhysRevA.72.062317](https://doi.org/10.1103/PhysRevA.72.062317)
8. H. Schmitz, R. Matjeschk, Ch. Schneider, J. Glueckert, M. Enderlein, T. Huber, T. Schaetz, Quantum walk of a trapped ion in phase space. *Phys. Rev. Lett.* **103**, 090504 (2009). [doi:10.1103/PhysRevLett.103.090504](https://doi.org/10.1103/PhysRevLett.103.090504) [Medline](#)
9. P. Richerme, Z.-X. Gong, A. Lee, C. Senko, J. Smith, M. Foss-Feig, S. Michalakis, A. V. Gorshkov, C. Monroe, Non-local propagation of correlations in quantum systems with long-range interactions. *Nature* **511**, 198–201 (2014). [doi:10.1038/nature13450](https://doi.org/10.1038/nature13450) [Medline](#)
10. V. V. Ramasesh, E. Flurin, M. Rudner, I. Siddiqi, N. Y. Yao, Direct probe of topological invariants using Bloch oscillating quantum walks. *Phys. Rev. Lett.* **118**, 130501 (2017). [doi:10.1103/PhysRevLett.118.130501](https://doi.org/10.1103/PhysRevLett.118.130501) [Medline](#)
11. M. Karski, L. Förster, J.-M. Choi, A. Steffen, W. Alt, D. Meschede, A. Widera, Quantum walk in position space with single optically trapped atoms. *Science* **325**, 174–177 (2009). [doi:10.1126/science.1174436](https://doi.org/10.1126/science.1174436) [Medline](#)
12. P. M. Preiss, R. Ma, M. E. Tai, A. Lukin, M. Rispoli, P. Zupancic, Y. Lahini, R. Islam, M. Greiner, Strongly correlated quantum walks in optical lattices. *Science* **347**, 1229–1233 (2015). [doi:10.1126/science.1260364](https://doi.org/10.1126/science.1260364) [Medline](#)
13. M. Gong, M.-C. Chen, Y. Zheng, S. Wang, C. Zha, H. Deng, Z. Yan, H. Rong, Y. Wu, S. Li, F. Chen, Y. Zhao, F. Liang, J. Lin, Y. Xu, C. Guo, L. Sun, A. D. Castellano, H. Wang, C. Peng, C.-Y. Lu, X. Zhu, J.-W. Pan, Genuine 12-qubit entanglement on a superconducting quantum processor. *Phys. Rev. Lett.* **122**, 110501 (2019). [doi:10.1103/PhysRevLett.122.110501](https://doi.org/10.1103/PhysRevLett.122.110501) [Medline](#)

14. J. Zhang, G. Pagano, P. W. Hess, A. Kyprianidis, P. Becker, H. Kaplan, A. V. Gorshkov, Z.-X. Gong, C. Monroe, Observation of a many-body dynamical phase transition with a 53-qubit quantum simulator. *Nature* **551**, 601–604 (2017). [doi:10.1038/nature24654](https://doi.org/10.1038/nature24654) [Medline](#)
15. P. Roushan, C. Neill, J. Tangpanitanon, V. M. Bastidas, A. Megrant, R. Barends, Y. Chen, Z. Chen, B. Chiaro, A. Dunsworth, A. Fowler, B. Foxen, M. Giustina, E. Jeffrey, J. Kelly, E. Lucero, J. Mutus, M. Neeley, C. Quintana, D. Sank, A. Vainsencher, J. Wenner, T. White, H. Neven, D. G. Angelakis, J. Martinis, Spectroscopic signatures of localization with interacting photons in superconducting qubits. *Science* **358**, 1175–1179 (2017). [doi:10.1126/science.aao1401](https://doi.org/10.1126/science.aao1401) [Medline](#)
16. K. Xu, J.-J. Chen, Y. Zeng, Y.-R. Zhang, C. Song, W. Liu, Q. Guo, P. Zhang, D. Xu, H. Deng, K. Huang, H. Wang, X. Zhu, D. Zheng, H. Fan, Emulating many-body localization with a superconducting quantum processor. *Phys. Rev. Lett.* **120**, 050507 (2018). [doi:10.1103/PhysRevLett.120.050507](https://doi.org/10.1103/PhysRevLett.120.050507) [Medline](#)
17. E. H. Lieb, D. W. Robinson, Finite-group velocity of quantum spin systems. *Commun. Math. Phys.* **28**, 251–257 (1972). [doi:10.1007/BF01645779](https://doi.org/10.1007/BF01645779)
18. P. Jurcevic, B. P. Lanyon, P. Hauke, C. Hempel, P. Zoller, R. Blatt, C. F. Roos, Quasiparticle engineering and entanglement propagation in a quantum many-body system. *Nature* **511**, 202–205 (2014). [doi:10.1038/nature13461](https://doi.org/10.1038/nature13461) [Medline](#)
19. M. A. Cazalilla, R. Citro, T. Giamarchi, E. Orignac, M. Rigol, One dimensional bosons: From condensed matter systems to ultracold gases. *Rev. Mod. Phys.* **83**, 1405–1466 (2011). [doi:10.1103/RevModPhys.83.1405](https://doi.org/10.1103/RevModPhys.83.1405)
20. M. S. Underwood, D. L. Feder, Bose-Hubbard model for universal quantum-walk-based computation. *Phys. Rev. A* **85**, 052314 (2012). [doi:10.1103/PhysRevA.85.052314](https://doi.org/10.1103/PhysRevA.85.052314)
21. J. Q. You, X. D. Hu, S. Ashhab, F. Nori, Low-decoherence flux qubit. *Phys. Rev. B* **75**, 140515 (2007). [doi:10.1103/PhysRevB.75.140515](https://doi.org/10.1103/PhysRevB.75.140515)
22. J. Koch, T. M. Yu, J. Gambetta, A. A. Houck, D. I. Schuster, J. Majer, A. Blais, M. H. Devoret, S. M. Girvin, R. J. Schoelkopf, Charge-insensitive qubit design derived from the Cooper pair box. *Phys. Rev. A* **76**, 042319 (2007). [doi:10.1103/PhysRevA.76.042319](https://doi.org/10.1103/PhysRevA.76.042319)
23. R. Barends, J. Kelly, A. Megrant, A. Veitia, D. Sank, E. Jeffrey, T. C. White, J. Mutus, A. G. Fowler, B. Campbell, Y. Chen, Z. Chen, B. Chiaro, A. Dunsworth, C. Neill, P. O’Malley, P. Roushan, A. Vainsencher, J. Wenner, A. N. Korotkov, A. N. Cleland, J. M. Martinis, Superconducting quantum circuits at the surface code threshold for fault tolerance. *Nature* **508**, 500–503 (2014). [doi:10.1038/nature13171](https://doi.org/10.1038/nature13171) [Medline](#)
24. E. Lucero, J. Kelly, R. C. Bialczak, M. Lenander, M. Mariantoni, M. Neeley, A. D. O’Connell, D. Sank, H. Wang, M. Weides, J. Wenner, T. Yamamoto, A. N. Cleland, J. M. Martinis, Reduced phase error through optimized control of a superconducting qubit. *Phys. Rev. A* **82**, 042339 (2010). [doi:10.1103/PhysRevA.82.042339](https://doi.org/10.1103/PhysRevA.82.042339)
25. K.-Q. Huang, Q. Guo, C. Song, Y. Zheng, H. Deng, Y. Wu, Y. Jin, X. Zhu, D. Zheng, Fabrication and characterization of ultra-low noise narrow and wide band Josephson parametric amplifiers. *Chin. Phys. B* **26**, 094203 (2017). [doi:10.1088/1674-1056/26/9/094203](https://doi.org/10.1088/1674-1056/26/9/094203)

26. M. Cheneau, P. Barmettler, D. Poletti, M. Endres, P. Schauss, T. Fukuhara, C. Gross, I. Bloch, C. Kollath, S. Kuhr, Light-cone-like spreading of correlations in a quantum many-body system. *Nature* **481**, 484–487 (2012). [doi:10.1038/nature10748](https://doi.org/10.1038/nature10748) [Medline](#)
27. W. K. Wootters, Entanglement of formation of an arbitrary state of two qubits. *Phys. Rev. Lett.* **80**, 2245–2248 (1998). [doi:10.1103/PhysRevLett.80.2245](https://doi.org/10.1103/PhysRevLett.80.2245)
28. T. Fukuhara, P. Schauß, M. Endres, S. Hild, M. Cheneau, I. Bloch, C. Gross, Microscopic observation of magnon bound states and their dynamics. *Nature* **502**, 76–79 (2013). [doi:10.1038/nature12541](https://doi.org/10.1038/nature12541) [Medline](#)
29. S. Bravyi, M. B. Hastings, F. Verstraete, Lieb-Robinson bounds and the generation of correlations and topological quantum order. *Phys. Rev. Lett.* **97**, 050401 (2006). [doi:10.1103/PhysRevLett.97.050401](https://doi.org/10.1103/PhysRevLett.97.050401) [Medline](#)
30. Y. Lahini, M. Verbin, S. D. Huber, Y. Bromberg, R. Pugatch, Y. Silberberg, Quantum walk of two interacting bosons. *Phys. Rev. A* **86**, 011603 (2012). [doi:10.1103/PhysRevA.86.011603](https://doi.org/10.1103/PhysRevA.86.011603)